THESIS FOR THE DEGREE OF DOCTOR OF PHILOSOPHY (Ph.D.)

Characterization of normal and pathological patterns of diffusion anisotropy with diffusion tensor imaging

by András Jakab M.D.

Supervisor: Ervin Berényi M.D. Ph.D.

UNIVERSITY OF DEBRECEN
DOCTORAL SCHOOL OF NEUROSCIENCES

DEBRECEN, 2012

Table of contents

Abbreviations

ACC: anterior cingulate cortex
ADC: apparent diffusion coefficient
ANN: artificial neural network
BAT: brain adjacent to tumor
CNS: central nervous system
COG: center of gravity
DF: discriminant function
DLPFC: dorsolateral prefrontal cortex
dMRI: diffusion magnetic resonance imaging (i.e. DWI and DTI)
DTI: diffusion tensor imaging
DWI: diffusion weighted imaging
EPI: echo planar imaging
FLAIR: Fluid Attenuated Inversion Recovery
fMRI: functional magnetic resonance imaging
FOV: field of view
FSL: Functional Magnetic Resonance Imaging of the Brain Software Library
HGG: high grade glioma
HGPM: high grade probability map
LGG: low grade glioma
LGPM: low grade probability map
MD: mean diffusivity
MD: mediodorsal thalamic nucleus
MDA: multivariate discriminant analysis
MDmc: mediodorsal thalamic nucleus, magnocellular part
MDpc: mediodorsal thalamic nucleus, parvocellular part
MPG: multiple pulsed gradient
MNI: Montreal Neurological Institute
MRI: magnetic resonance imaging
NKI: Nathan Kline Institute
NMR: nuclear magnetic resonance
ROI: region of interest
TE: echo time
TPM: tumor probability map
TR: repetition time
UD-MHSC: University of Debrecen, Medical and Health Science Center
WHO: World Health Organization

1. Introduction

Water is a fundamental and ample constituent of all living creatures and it is an almost trivial statement that tissue water is structured according to the characteristics and intrinsic features of any given tissue type. This is undoubtedly the rationale of modern magnetic resonance technologies that dominated the field of biomedical and diagnostic imaging of the central nervous system for the last two decades. The initial and nearly prophetic enthusiasm about this technique led to anticipations that the ubiquitous nuclear magnetic resonance (NMR) phenomenon of tissues of the human body could reveal previously unseen details of pathologic processes; this could be done by characterizing the relaxation properties of spin systems. Here I shortly refer to an early patent of Raymond Damadian from 1972 in which he described a new design of an NMR device denoted as “Apparatus and method for detecting cancer in tissue” [1]. He correctly predicted that such scanners could pinpoint changes in tissue qualities that are brought about by neoplastic transformation.

One attribute of the uniquely organized pattern of water molecules is their diffusion characteristics. As we will elucidate in the thesis, a new family of imaging technologies was built upon this phenomenon, namely diffusion magnetic resonance imaging (dMRI). The date of this work – 2012 – hallmarks the 25th anniversary of diffusion MRI. Since the first depiction of the diffusion process in the human brain significant conceptual and methodological developments have been applied to dMRI [2]. While the spatial resolution of MR images is typically on the range of a millimeter, a strikingly unique feature of diffusion MRI approaches is that they probe the motion of water molecule systems that are happening on the micrometer scale. This theoretically means a way to sample the microarchitecture of tissue or subcellular water compartments which is extensively used as the rationale of diffusion MRI augmented research.

A significant part the thesis focuses on the application of diffusion tensor magnetic resonance imaging and related image processing techniques to characterize normal diffusion anisotropy patterns in the human brain. Such work is realized by the possibility to visualize and quantify the uniquely ordered structure of the brain’s white matter through probing the anisotropic water diffusion. This late twentieth century technique resurrects the explorations of the nineteenth century anatomists Theodor Meynert or Joseph Jules Dejerine who attributed a prominent role to white matter and fiber pathways in normal and pathological

brain functioning [3, 4]. We aim to demonstrate that diffusion MRI can be used for similar explorations but at a new level by portraying the connectional anatomy of living human subjects and relatively large cohorts. First, we explore the topography of diffusion anisotropy and structural connections of the human insula, then similar dissections for the mediodorsal thalamic nucleus are provided.

The second part of our investigations focuses on the anisotropy patterns of diffusion in pathological conditions, more specifically, to portray the diffusion characteristics in brain neoplasms of glial origin. The most prevalent forms of brain tumors are glial neoplasms whereas astrocytic tumors constitute the majority of gliomas, as stated by the last World Health Organization (WHO) classification [5]; however, mixed cellular composition is also common [6]. Separating gliomas into low-grade and high-grade classes has become the means for assessing the neoplastic biological behavior and this partitioning fundamentally determines therapy and patients' survival. Treatment of brain tumor patients remains a major challenge of oncology despite revolution of diagnostics and surgical therapies. The ability of diffusion MRI to probe the tissue microstructure may give hope for developing new radiological image processing methods that finally pinpoint early changes in the neoplastic transformation of the brain.

2. Background and review of literature

Early pioneers of nuclear magnetic resonance (NMR) research described that it is possible to sensitize the MR signal to the motion of water molecules that is caused by their self-diffusion [7]. By the same token, MR imaging sequences were developed that not only pictured different components of the spins' relaxation phenomena but responded to the microscopic displacements driven by diffusion, taking place in living tissues during the acquisition of images. Hence diffusion-weighted magnetic resonance measurements provide non-invasive description of in vivo diffusion within elementary image units, voxels [8]. The most commonly used parameter to describe the self-diffusion process during dMRI is the apparent diffusion coefficient (ADC). The common way to calculate this formulation of the diffusion coefficient is to acquire images with and without the pulsed gradients switched on. The directionality of these gradients determine the axis where the apparent diffusion coefficient is measured; the average degree of the diffusion appearing along the X, Y and Z directions is simply referred to as average apparent diffusion coefficient, or again, ADC (or

aADC in other terminology). The relationship between the signal intensity on diffusion-weighted images and the apparent diffusion coefficient is formalized in the following equation.

Eq. 1. $SI_{DWI} = SI_{T2} * e^{-b*ADC}$

Where SI_{DWI} is the signal intensity of the voxels on the DWI images, SI_{T2} means the signal intensity on T2 acquisitions (B_0 images). ADC is the apparent diffusion coefficient while b is the parameter reflecting the strength of diffusion weighting.

In a glass of water, any water molecule covers the same distance per unit time in all directions of space and this isotropic diffusion is represented by a sphere. Such movement is only governed by fundamental physical parameters such as the size of particles, the viscosity and the absolute temperature (as formalized by the well-known "Stokes-Einstein" equation). In living systems the tissue structure determines the movement of the same molecule, i.e., the diffusion properties and its magnitude as well. The result of this phenomenon is called anisotropic diffusion where the diffusion profile (i.e. the profile of propagation of water molecules) can be described by amorphous 3D or ellipsoid geometric solids. Various proteins, membranes, cytoskeletal and extracellular matrix elements play an important role in characterizing and determining the movement (diffusivity) of water molecules. Such elements act as "obstacles", subsequently modify the diffusion profile and hinder or restrict the movement of molecules. Given its specially organized cellular and tissue microarchitecture, the central nervous system already gained prominent attention in the pioneering times of diffusion MRI research. It was discovered that the intravoxel incoherent motion of water molecules shows significant directional preference in white matter when diffusion sensitizing gradients are applied and that such direction dependent changes of contrast patterns putatively match our previous knowledge about the distribution of major fiber tracts [9]. Since then, a great effort was invested into elucidating the main source of this highly ordered anisotropy in the white matter of the brain [10]. It is safe to conclude from such studies that the main component which contributes to the anisotropic patterns observed in white matter is the dense packaging of axonal membranes and that the myelin sheath or intracellular organs and proteins have minor influence.

2.1. Basics of diffusion tensor imaging

The direct consequence of the hindered self-diffusion of water molecules in the brain – especially in the white matter – is that the observed magnitude of diffusion (i.e. the apparent diffusion coefficient) greatly varies depending of the direction of the pulsed gradient used. To formalize this direction-dependence of the diffusion process, Basser and Pierpaoli used tensors and suggested the use of quantitative diffusion tensor MRI to characterize microstructural and physiological features of tissues [11]. Diffusion tensor imaging (DTI) has increased sophistication over diffusion-weighted MRI since DTI data have information on the magnitude and orientation of anisotropic diffusion as well. In such models, the diffusion process is not characterized by a single scalar coefficient but by a symmetric tensor, $\underline{\mathbf{D}}$ that describes displacements of water molecules along each axis (D_{xx}, D_{xy}, etc.) and the correlation between displacements along these axes are formalized in the following equation:

Eq. 2.
$$\underline{D} = \begin{matrix} D_{xx} & D_{xy} & D_{xz} \\ D_{xy} & D_{yy} & D_{yz} \\ D_{xz} & D_{yz} & D_{zz} \end{matrix}$$

This equation forecasts that it is theoretically feasible to obtain all the components of the diffusion tensor with diffusion MRI by acquiring images sensitized to 6 different diffusion directions. This is achieved by the combination of motion sensitizing gradient pulses along the X, Y and Z axes [2, 11]. When acquiring such images, the signal attenuation is given by the following equation:

Eq. 3.
$$A = \exp\left(-\sum_{i=x,y,z}\sum_{j=x,y,z} \underline{b}_{ij} * \underline{D}_{ij}\right)$$

Where A is the signal attenuation, b_{ij} are the elements of a $\underline{\boldsymbol{b}}$ matrix and D_{ij} are the elements of the matrix mentioned previously.

In order to ease the display of such tensorial data, the concept of diffusion ellipsoids were proposed. This ellipsoid is understood as the three-dimensional representation of the diffusion distance that is covered by molecules in a given diffusion time. It is calculated by "diagonalizing" the diffusion tensor for each image voxel. Diagonalization results in the so-called principal eigenvector of the tensor, which is the vector where the diffusion appears to have the largest magnitude. Furthermore, the ellipsoid is characterized by three eigenvalues that describe the extent of the three orthogonal axes. The eigenvalue of the principal

eigenvector is denoted with λ_1, while the orthogonal components of the ellipsoid are given as λ_2 and λ_3. The tensor dataset and eigenvalues are fundamental in the calculation of secondary images, such images allow us to visualize various diffusion characteristics as grayscale images and enable thorough statistical analysis. The most commonly used DTI parameters are the following. Mean diffusivity (MD) characterizes the overall mean-squared displacement of molecules (average ellipsoid size) and the overall presence of obstacles to diffusion. One way to describe the degree of anisotropy is to calculate the fractional anisotropy (FA) measure, this parameter depicts how much molecular displacements vary in space (eccentricity of the ellipsoid) and is related to the coherence of oriented structures. The spatial orientation of the structures is described by the main direction of diffusivities (main ellipsoid axes) and referred to as the longitudinal diffusivity (along the axis of the principal eigenvector) or perpendicular diffusivity.

2.2. Characterization of normal anatomical connectivity patterns in the human brain

From the perspective of neuroanatomy research, mapping the structural (i.e. anatomical) connections is interesting as the inflow or output of information available to a certain brain territory hallmarks its putative function and determines the influence it can has over other areas [12]. Given that in brain tissue the densely packed axons are the main sources of the diffusion anisotropy, such tensors readily describe the orientation of the dominant fiber population in each voxel [10]. Major fiber bundles can be visualized by means of fiber tracking. For this purpose, many algorithms were suggested, introducing a previously unseen field of biomedical visualizations aiming to depict the anatomy of fiber paths in vivo [13, 14]. The initial enthusiasm about this tool as a modality for in vivo virtual dissections of white matter anatomy was later transformed to an effort aiming to validate these re-discovered neuronal pathways [15]. This was mainly done by means of more conventional neuroanatomical approaches [16, 17]. Additionally, it became clear that newer computational methods are required to describe the complex intra-voxel distribution of axonal populations, such as mapping the propagation of uncertainty of possible fiber trajectories, one of the techniques denoted as probabilistic tractography [18]. The science of connectional anatomy – hodology – was recently electrified by the advent of fiber tractography and mapping techniques [19]. A probabilistic approach to trace the structural connections along trajectories that are defined by the diffusion modeling now allows to reveal tracts even adjacent to the cortex, or event depict the connections that arise primarily from cortical regions. We

hypothesize that a plausible work flow can be implemented that uses DTI data and allows studying the normal connectional anatomy of the human cerebral cortex. Our first special focus is on mapping the human insular cortex by in vivo diffusion MRI.

The insula of Reil, located deeply within the lateral sulcus, is known to have a multifaceted sensory, motor, visceral and cognitive role and is also considered as a vestibular association area. The insular cortex is acknowledged as the anatomical representation for interoceptive awareness, i.e., the "sense of the physiological condition of the body" [20]. Its functional and anatomical diversity has been described in humans and non-human primates [21], with changes in cytoarchitecture that follow a rostroventral to dorsal and posterior gradient, from agranular to dysgranular and granular cortex [22, 23]. In humans, functional neuroimaging studies by means of resting-state functional MRI (fMRI) have been recently used to reinvigorate the relationship of morphology and function of the insula by demonstrating consistent changes of patterns of activation or functional connectivity [24]. Cauda and colleagues demonstrated the functional connectivity of the insula to various cortical and subcortical targets by quantifying the similarities between time coursers of functional activations and using this information to reveal coherent connectivity networks. Their findings on this functional connectivity revealed two major complementary networks involving the ventral-anterior and dorsal-posterior insula. One network connects the anterior insula to the middle and inferior temporal cortex and anterior cingulate cortex, and is believed to be related to limbic regions which play a role in emotional aspects. The second links the middle-posterior insula to premotor, sensorimotor, supplementary motor and middle-posterior cingulate cortices, indicating a role for the insula in sensorimotor integration [24].

Diffusion tensor imaging offers remarkable possibilities to explicate the properties of the hindered biological diffusion while tractography depicts structural connectivity within distinct brain regions. Diffusion-based techniques provide the possibility to parcellate the gray matter according to its local diffusion properties [25], either by quantifying the connection strengths to predefined cortical areas [26], or more generally, to compute similarities between connections to remote areas [27]. During this approach, structural connectivity is traced from areas of the cortex with probabilistic diffusion tractography and sub-domains are identified that present a demarked pattern of connections. Johansen-Berg and co-authors demonstrated rapid spatial changes in the connectivity profile between the supplementary motor area (SMA) and the pre-SMA, offering an in vivo method to delineate them on an individual basis.

Similarly, the technique has already been applied to segment the insula: Nanetti and colleagues revealed a rostrocaudal variation of connectivity-based segments dividing the insula into two clusters, while Cerliani et al. refined this picture by reporting a more gradual change of connectivity patterns along this axis [28, 29]. Our report aims to describe two separated regions within the left and right insula that are defined by clustering insular image voxels based on their distant cortical connections. Furthermore, we aim to provide evidence for interhemispheric variability of the clusters in terms of spatial location, overall volume and micro-structural properties of diffusion, for this purpose, we aim to use a cohort of healthy volunteers.

Diffusion tensor imaging augmented with a probabilistic framework of fiber tractography allows mapping thalamocortical (or corticothalamic) connections noninvasively. This observation gave rise to a number of studies on the normal human thalamus anatomy or its putative alterations in pathological conditions [26, 30]. A novel way to picture structural connections of the thalamus is to delineate and define regions based on their primary sources of afferent or efferent connections [31]. This technique potentially depicts groups of thalamic nuclei that are different in terms of interconnections to the cortex or other, pre-defined "target" regions. We highlight that connectivity-based segmentation has already passed tests of reproducibility [32, 33], applicability in functional neurosurgical planning and correlation to neurophysiological mapping [34, 35]. We hypothesize that such approach can be used to demonstrate the connectional anatomy of the human thalamus mediodorsal nucleus in a relatively large population of healthy volunteers.

Endeavors to study the role of the mediodorsal thalamic nucleus (MD) already postulated it as a possible association hub mediating affective and cognitive functions [36]. In non-human primates, evidence comes from a wide range of works describing the interconnections of the MD nucleus with several cortical areas, predominantly with the prefrontal cortex [37-39]. Changes of connectivity patterns were found to be coherent with the classical cytoarchitectural subdivisions of the MD, with the medial and orbital prefrontal regions projecting to the medial sector (magnocellular part) and fibers of the dorsolateral prefrontal cortex projecting to the lateral sector (parvocellular part) in experimental animals [40-42]. Many clinical studies support the active participation of the mediodorsal nucleus in higher cognitive functioning, although these investigations mainly concentrated on linking the

impairment of cognitive and executive performance to anatomical locations of intrathalamic lesions or to volume changes in epilepsy [43-45].

The impetus for the second part of our study was that in vivo neuroimaging methods have successfully been applied to study the connectional anatomy of the mediodorsal nucleus, and compelling similarity to the primate thalamocortical networks was revealed [31]. We aimed to perform connectivity-based parcellation to reveal subdivisions within the human mediodorsal thalamic nucleus by automatically delineating areas that show distinct remote connectivity profiles. Our study was designed to unveil the interhemispheric differences and intersubject variability in the extent of such connectivity-based domains, for this purpose, we accessed the images of a large number of healthy subjects. We assumed that the macroscopic anatomy of such subdivisions provide further information on the functional specialization of the MD nucleus. This idea stems from the fact that structural connectivity determines the territories from where information could reach an area while the efferent connections limit the regions which it can directly influence [12]. Therefore, keeping in mind its limited capabilities in depicting finely detailed anatomy, we can use tractography-based charting of gray matter to obtain information not only about local features, but also about more remote trajectories and large circuits passing through that region [15]. The neuroanatomical model of segregated "cortico-striato-thalamo-cortical" networks forms the basis for our hypothesis, in which circuitry the mediodorsal thalamic nucleus was found to play an intermediary role [46]. Neuroimaging studies show that macroscopic anatomical features (e.g., total gray matter volume of frontal lobe) show correlation with the intellectual abilities of the individual [47, 48]. By the same token, individual, imaging-based and connectionist definition of anatomical features can be investigated as neuroanatomical correlates of higher cognitive functions. We conclude that an initial step in such explorations is to provide normative data on the anatomy of humans, preferably using large subject populations and in vivo imaging techniques.

2.3. Characterization of pathological diffusion anisotropy patterns in the human brain

As previously described, the highly anisotropic appearance of diffusion in the central nervous system is predominantly caused by the dense packaging of ordered axonal membranes in white matter [10]. Further components might influence such patterns by hindering the diffusion: intracellular proteins, microtubules, neurofilaments, extracellular matrix components and the myelin sheath of neurons. In case of changing intra- and extracellular structure, for instance the disorganization that accompanies neoplastic

transformation, the diffusion characteristics are bound to be altered. Therefore diffusion imaging putatively probes the biological microarchitecture and offers hope to correlate such measurements with tissue properties in pathological conditions or even to reveal the peculiar microstructure of neoplastic tissue.

Diffusion data are often correlated with cellular physiology and tissue microstructure, and has extensively been used in the studies of central nervous system gliomas. Here we report the latest findings in glioma imaging from the perspective of diffusion MRI applications, with attention to studies that focused on diffusion derived parameters such as mean diffusivity or fractional anisotropy. Furthermore, we present the body of literature that supports the feasibility of diffusion MRI in the determination of glioma WHO grade or separate low and high grade gliomas. Mean diffusivity measures allowed differentiation and outlining the central necrotic areas within high-grade gliomas as well as separating peritumoral edema from adjacent WM structures; however, tumor infiltration cannot be evaluated properly [49, 50]. A strong correlation between tumor cellularity and the apparent diffusion coefficient (ADC) may also help to estimate tumor grade [51, 52]. The reliability of this grade assessment method, however, is questionable primarily due to a great deal of subjectivity involved in histological tumor typing [53]. Meanwhile, data on the association between fractional anisotropy values and tumor characteristics, including WHO grade are also available. Co-analysis of tensor-related parameters also provides basis for such correlative conclusions [54-56]. Combination of variables referring to the apparent diffusion coefficient in gliomas (e.g. minimum and maximum value of ADC) and multiparametric approaches facilitate tissue characterization and classification [57, 58]. Use of histograms for studying distributions of different parameters further improves identification of tumor subtypes [59, 60]. Despite the endeavors to use conventional MRI for the delineation of high-grade gliomas, low sensitivity and specificity was reported [61]. When compared to region of interest analysis, construction of histograms to represent the distribution of voxels' values in a tumor was more feasible whilst this approach allowed successful grading of gliomas [62]. Dehmeshki and co-authors described that discriminant analysis (DA) is capable of selecting the most important features of individual image histograms for classifying cases in different pathologies; a practical representation of such features is calculating histogram bins for each case [63, 64]. Imaging results have already been interpreted as adequate indicators of not only WHO histopathology types (classification), but also as descriptors of tumor pathophysiology (proliferation, metabolism, blood flow). Comparing FA values, mean diffusivity to

histopathological evaluation of biopsy samples of glioblastoma multiforme tumors proved a consistent relationship between the radiology data and tumor cellularity as well as radiology measures and the Mib-1 LI (labeling index, assessed with the monoclonal antibody for Ki-67) [65, 66]. Further extension of non-invasive tumor evaluation needs to keep in sight those striking results which dominate the current neuro-oncopathology literature. It has recently become obvious that in addition to traditional morphology molecular features often allow estimates of not only disease prognosis but also prediction. The latter activity determines individual tumor sensitivity towards a specific chemotherapeutical regimen [67, 68].

Various studies on the relationship between imaging parameters and pathology aim to develop new ways of depictions that can help to characterize tumors. Nosology – the discipline dealing with the classification of diseases – was reinterpreted by Szabo De Edelenyi in his report where he uses this term to introduce a new form of an imaging-based parametric map [69]. According to this terminology, nosological maps depict the probability of the occurrence of certain disease subtypes for each image voxel, based on the image features (typically multidimensional) underneath that particular voxel. Such visualizations potentially ease the interpretation of multispectral data, such as proton magnetic resonance spectroscopic images or diffusion tensor datasets. Literature shows that it is possible to visualize biologically diverse regions within a tumor based on image analysis and various modeling approaches; a method was reported that depicts histopathological subtypes (i.e. “oligo-like” or “astro-like” regions, according to the authors' nomenclature) of low-grade gliomas as color maps [70]. Similarly, “nosological images” graphically represented different tumor types by performing complex interpretation of MR spectroscopy data and it was practical to use T2 and ADC values for tumor xenograft characterization by segmenting tumor images into various sub-populations [69, 71, 72].

Such works form the basis of our next hypothesis that machine-learning algorithms are capable of integrating information from preoperative images whilst multidimensional pattern-recognition techniques could enhance the characterization of gliomas. A practical approach is supervised learning where previously determined ground truth is provided by histopathology and mathematical models are optimized for finding the correlation of individual, subject-based data and the tumor classification. One such method, the artificial neural networks (ANN) has long been investigated as a potential candidate for oncology decision support finding more specific aims as brain tumor classification [73-76]. By the same token, our

investigation was designed to introduce a new visualization method that portrays glioma grade by incorporating information from postgadolinium T1- and T2-weighted, diffusion-weighted and parametric images that were computed from diffusion-tensor measurements. We focused on the development of an imaging biomarker that estimates tumor grade by employing a voxel-wise computational approach based on a supervised learning algorithm.

2.4. Study aims

The primary motivation of the study was to employ *in vivo* diffusion tensor imaging to portray individual anisotropy patterns of cerebral water diffusion in physiological and pathological scenarios. We aimed to demonstrate the applicability of DTI data analysis to study the normal human anatomy in a relatively large subject population. Furthermore, to retrospectively analyze a patient group with brain gliomas to reveal a possible neuro-oncological application of DTI. The experiments were designed to elucidate the following topics, each denoted as a specific (major) aim or secondary (minor) aims.

A. To show the applicability of DTI to study the connectional anatomy of the human cerebral cortex, with special focus on the insula.

   A/1. To use probabilistic diffusion tractography to map the macroscopic structural connections of the insular cortex.
   A/2. To use such data to reveal subdomains within the human insular cortex that are automatically defined by analyzing the patterns of remote connections.
   A/3. To analyze the distribution, location and interhemispheric asymmetry of such connectivity-based insular subdomains and to measure the microstructural properties of water diffusion within the newly defined areas.
   A/4. To compare the subdomains based on the analysis of diffusion anisotropy and tensor data with the classical depictions of major cytoarchitectural domains.

B. To show the applicability of DTI to study the connectional anatomy of the human thalamus, with special attention to the mediodorsal nucleus.

   B/1. To employ probabilistic diffusion tractography to trace the interconnections between the human mediodorsal thalamic nucleus and the cerebral cortex.
   B/2. Similarly to specific aims A/2 and A/3, to define subdomains in the mediodorsal nucleus based on the patterns of remote connectivity.
   B/3. To compare the neuroanatomy of the connectionist definition of the subdomains of the mediodorsal nucleus with the cytoarchitectural subdivisions.

C. To use DTI to characterize the spatial patterns of diffusion anisotropy within CNS gliomas and correlate such findings with histological features that are used to type gliomas.

C/1. To assess the feasibility of using preoperatively acquired DTI images to grade gliomas.

C/2. To develop a graphical representation of the imaging-based interpretation of glioma grade.

3. Materials and methods

3.1. Study subjects

In accordance with the aims (A, B and C) defined previously, three different cohorts of subjects were enrolled in the study. For aim A, data of healthy volunteers were accessed from the repository of a national collaborator (University of Kaposvár), while for aim B, we used the publicly available Rockland Neuroimaging Sample provided by the Nathan Kline Institute (NKI, Orangeburg, USA). The original NKI sample consisted of the images of 210 subjects, which was sampled and reduced to 155 subjects to have a more homogeneous population (according to the criteria outlined in Table 1.). This sample is a freely available, large-scale, extensively phenotyped dataset for the purpose of discovery science and contains healthy subjects from nearly all age groups. The general characteristics and the inclusion criteria of the study populations for specific aims A and B are summarized in Table 1.

Name of specific aim served, dataset	Subjects	Gender (male/female)	Age (mean ± SD)	Selection criteria	Source of subjects
Specific aim A	40	19/21	33.8 ± 12.7	Right-handed, healthy adults	University of Kaposvár
Specific aim B	155	92/59	38.8 ± 19.4	Right-handed healthy subjects, age range 14-65 years, available IQ data and DTI	Rockland Sample, Nathan Kline Institute
Specific aim C	40	18/22	38.6 ± 16.6	WHO grade II-IV gliomas, DTI scans available, no prior treatment	UD-MHSC

Table 1. Subject characteristics and selection criteria for specific aims A-C.

Aim C required retrospective data analysis of patients with CNS gliomas and the construction of a dataset that was determined by the availability of an adequate pre-operative radiological workup including diffusion tensor imaging acquisitions. We collected the images and basic clinical data of 40 consecutive subjects meeting the inclusion criteria, diagnosed with brain gliomas between 2006 and 2010. Cases were labeled according to WHO grade (Gr. II: 26, Gr. III: 3, Gr. IV: 11) and were also divided into low and high grade classes. All tumors were histologically classified using either stereotactic biopsy material or specimens of

surgical debulking (Institute of Pathology, UD-MHSC). The original diagnoses were reviewed blind to the results of radiological analysis. Inclusion criteria were the availability of DTI scans and only those glial tumors were selected which had been sampled prior to any kind of treatment (i.e., surgical removal, radiotherapy or cytostatic therapy). Patient baseline characteristics and a summary of the histopathological diagnoses of the subjects' tumors are demonstrated in Table 2.

Tumor histopathology	**Subjects**	**Gender (male/female)**	**Age (mean ± SD, range)**
Low grade tumors	**26**	**13/13**	**34.6 ± 15.9 (8-68)**
astrocytoma gr. II. or astrocytoma fibrillare gr. II.	13	7/6	30.6 ± 16.9 (8-59)
oligoastrocytoma gr. II.	7	¾	37.9 ± 18.4(11-68)
oligodendroglioma gr. II.	6	3/3	42.2 ± 9.9 (34-59)
High grade tumors	**14**	**5/9**	**47.3 ± 15.4 (13-68)**
oligoastrocytoma gr. III.	3	0/3	52.0 ± 2.6 (50-55)
glioblastoma multiforme	11	5/6	45.7 ± 17.6 (13-68)
Overall	**40**	**18/22**	**38.6 ± 16.6 (8-68)**

Table 2. Preoperative assessment of glioma grade through the analysis of diffusion tensor images (specific aim C): subject baseline characteristics and histopathological composition of the subjects' tumors.

During the construction of each dataset, participants gave informed written consent to procedures approved by the relevant Institutional Review Boards. Further information of the study cohort for specific aim B is provided on the website of the International Neuroimaging Data-sharing Initiative, the INDI [77].

3.2. Image acquisition protocols

Due to the fact that three institutions contributed to the imaging datasets of the study, I report the MRI acquisition protocols according to the specific aim served by the relevant scans of the institutions. As a general rule, high-resolution anatomical, T1-weighted imaging

was performed for each subject in each cohort, which was complemented by diffusion tensor imaging. Details of the MRI and DTI acquisitions are given in Table 3.

		Specific aim A	Specific aim B	Specific aim C
	Institution	University of Kaposvár	Nathan Kline Institute	UD-MHSC
	Scanner type (Field strength, vendor)	1.5 T MRI system (MagnetomAvanto, Siemens, Erlangen, Germany)	3.0 T MRI system (Magnetom Trio Tim, Siemens, Erlangen, Germany)	1.5 T MRI system (GE Signa Excite TwinGradient, GE Medical Systems, Milwaukee, WI)
Anatomical imaging	**Applied sequence**	3DT1 MPRAGE (native)	3DT1 MPRAGE (native)	3DT1 SPGR (Gadolinium contrast agent administration)
	TE/TR	4.2 / 1160 ms	3.5 / 2500 ms	6 / 21 ms
	Image matrix	384 * 512	256 * 256	512 * 512
	Voxel size	0.45 * 0.45 * 0.83 mm	1 * 1 * 1 mm	0.68 * 0.68 * 1.1 mm
Diffusion tensor imaging	**Applied sequence**	Spin echo EPI	Spin echo EPI, GRAPPA parallel imaging (acceleration factor: 3)	Spin echo EPI
	TE/TR	118 / 10000 ms	91 / 10000 ms	98 / 10000 ms
	MPG	12	64	25
	b-factor	1000 s/mm^2	1000 s/mm^2	1000 s/mm^2
	Voxel size	1 * 1 mm	2 * 2 mm	1.5 * 1.5 mm
	Slice thickness	3 mm	2 mm	3.3 mm

Table 3. Anatomical MRI and DTI acquisition protocols used for the subject cohorts of specific aims A-C. FOV: field of view, EPI: echo planar imaging, TR: repetition time, TE: echo time, MPG: number of multiple pulsed gradients.

3.3. Image and data processing protocols

3.3.1. Calculating the microstructural descriptors of diffusion

The acquisition of raw, diffusion weighted images allowed the voxel-wise estimation of the diffusion tensors for each subject. The diffusion tensor is described by the principal

eigenvector and three eigenvalues. To formulate the tensors based on the DWI data we relied on the built-in estimation algorithm of the FMRIB Diffusion Toolbox in the FSL software package (University of Oxford, [78]). All specific aims required the calculation of secondary images that are derived from the diffusion tensor; these are referred to as parametric or scalar images. The calculation of such parameters is extensively described by other studies; we refer to the technical reports and manuals of the applied algorithm, the *dtifit* (FMRIB Diffusion Toolbox. FSL, University of Oxford [78]). The following parametric maps were generated: B_0 images, which are acquired without diffusion sensitization thus conveying T2-weighted information; directionally averaged DWI images; fractional anisotropy maps (Eq. 4.); longitudinal (Eq. 5.) and radial diffusivity component maps (Eq. 6.), trace maps (Eq. 7.) and the MD (Eq. 8.). We used the following equations to calculate the parametric maps from the components of the diffusion tensor.

Eq. 4. $$FA = \sqrt{\frac{1}{2}} * \frac{\sqrt{(\lambda_1 - \lambda_2)^2 + (\lambda_1 - \lambda_3)^2 + (\lambda_1 - \lambda_3)^2}}{\sqrt{\lambda_1^2 + \lambda_2^2 + \lambda_3^2}}$$

Eq. 5. $\lambda \| = \lambda 1$

Eq. 6. $\lambda_\perp = (\lambda_2 + \lambda_3)/2$

Eq. 7. $\text{Trace} = \lambda_1 + \lambda_2 + \lambda_3$

Eq. 8. $\text{MD=ADC=} (\lambda_1 + \lambda_2 + \lambda_3)/3$

where λ_1, λ_2 and λ_3 are the three eigenvalues of the diffusion tensor. FA: fractional anisotropy. $\lambda_\|$: longitudinal diffusivity, $\lambda_\perp$: radial diffusivity.

3.3.2. In vivo mapping of connections with probabilistic diffusion tractography

To study the properties of normal connectional anatomy for specific aims A and B, the following processing steps of the DTI data were performed: (1) fitting a symmetric tensor to the DWI data and using the tensor's eigenvalues to calculate secondary, parametric maps, such as the fractional anisotropy image, (2) spatial standardization, i.e. registration of T1-weighted and DTI data to a standard neuroimaging template space, (3) estimation of intra-voxel distribution of fiber populations and (4) performing probabilistic tracking of structural connections arising from the investigated region. DTI processing steps were carried out using

the FMRIB Diffusion Toolbox in the FSL software package, we refer to this toolbox by naming the algorithm or built-in scripts used.

We performed non-linear spatial standardization of images to enable inter-subject comparison of anatomy. For each subject, the calculated fractional anisotropy images were used to determine a deformation field which transforms it to a common neuroimaging reference space (MNI space), namely the FMRIB58 fractional anisotropy template (distributed with the FSL tool). Image registration steps were done by accessing the *FLIRT* (initial, mutual information-based, linear registration with 12 degrees of freedom) and the *FNIRT* (non-linear warping) algorithm in the FSL software package. For anatomical images, the T1-weighted scans of each subject were transformed to the T1-weighted MNI152 template with the procedure described for the DTI standardization. Subsequently, anatomical images and tractography results were stored in a standard MNI152 neuroimaging space. This allowed to define the "seeding" masks (i.e., the volume from which probabilistic fiber tracing samples will emerge) for diffusion tractography by using only one template image for every subject assuming good anatomical overlaps, and therefore the tracking of neuronal connections were performed in the native diffusion spaces of individual subjects, only transforming the seeding masks and resulting images from and to the standard space.

The characterization of fiber distributions was carried out with a standard procedure, the *BedpostX* script. For more information on the probabilistic diffusion tractography procedure, see the relevant work by Behrens et al. [18]. This algorithm was set to search for two fiber populations in each image voxel in a way that the possible orientations of diffusion displacements best fit the observed raw, diffusion weighted data. Next, probabilistic tracking of structural connections were initiated by using the *ProbtrackX* program. The connection strength between each seeding voxel and every remote brain voxel was estimated as the probability of tracts reaching their target through a trajectory guided by the model of local diffusion characteristics. A non-linear registration was used to map the coordinates of seed voxels to the space of the diffusion images and then to project the tractograms back to the standard space. Each entry in such tractogram image shows the probability of that particular brain voxel to be interconnected to the seeding area.

3.3.3. Calculating the connectivity-based subdomains of the insular cortex

The specific aim A was to use the diffusion anisotropy data and diffusion tensors to study the connectional anatomy of the human cerebral cortex, with special focus on the insula. One way to study the connectional anatomy of the cortex is to perform the probabilistic tracking of structural connections from a specific seed area (aim A/1), and use this information to parcellate the original territory into subdomains that differ in terms of the patterns of connectivity (aim A/2). This “hodologist” definition of cortical of subcortical areas require a mathematical approach that separates such fiber trajectories and maps the origin of each fiber cluster back to the examined brain region. For studying the insula, we first accessed the mask of the insular cortex from the Harvard-Oxford Cortical Atlas (FSL), and then the T1-weighted image template in the MNI152 space was used to review and refine the borders of the insular cortex. The final region of interest (ROI) comprised only the band of gray matter voxels surrounded by the extreme capsule and the periinsular sulci.

Tractography was initiated from the reviewed insular cortical masks in the MNI152 space, with the procedure described in the report previously. We aimed to perform connectivity-based segmentation; hence an alternative way to store diffusion tractography results was applied, similarly to a number of works in this field [79-83]. For each subject, a connectivity matrix (M * N) was stored where each row (M) represented the seed voxels while the columns corresponding to the brain voxels (N), as stored in a low resolution, 4 * 4 * 4 mm space. This down-sampling was carried out to ease the computational and memory burden of the procedure. Elements of the matrix represented the probability of existing structural connections between corresponding seed and brain voxels. Next, a cross-correlation matrix was constructed (M * M), for each seed voxel quantifying the similarities of their connectivity patterns. Seed voxels were partitioned into two groups with a k-means clustering algorithm maximizing the within-group similarity of connection patterns (*Ccops* program, FSL). During the k-means algorithm, random initialization of cluster centers was employed, with an iterative search for the second cluster center to be the furthest away from the first; this method provides feasible within-subject reproducibility without performing multiple clustering, in contrast to other works [28]. Each voxel in the seed area (rows of the matrix) was assigned a label according to the cluster number it was classified previously. As this step was done in the standard neuroimaging space, the cluster membership labels were

consequently mapped back to the native space (T1-weighted anatomical) for each subject using the inverted spatial transformation of the standardization procedure.

In this paragraph, we report the methods that were used to evaluate and describe the anatomy of the newly formed connectivity-based subdivisions of the insular cortex, as outlined in the specific aim A/3. Based on the contours of each connectivity cluster, three-dimensional objects were formed and for each model the center of gravity point (COG) was determined in the MNI152 stereotactical space. The COG or the center of mass calculation was based on averaging the vertex coordinates of 3D meshes. This measure was done in order to reveal the spatial scatter of the connectivity-based domains through the study population. Hence the spatial consistency was measured as the scatter of COGs and the variability of absolute cluster volumes. For volumetric evaluations, each insular mask volume and its newly clustered partitions were transformed back to the subject's native anatomical space by using the inverted transformation of the standardization step (i.e. registration of the T1-weighted images to the MNI152 T1-weighted template). A population-averaged representation of the partitioning was computed by assigning the label value to each reference-space insular voxel that was most likely to be found in the individual cluster maps, i.e. the mode of the 4D object was determined. This 3D dataset of the most common cluster assignment was then used to create a 3D mesh for each cluster. To demonstrate the intersubject variability of the discovered clusters across the study population, we calculated and visualized images representing the 95th, 90th, 50th, 10th and 5th percentiles of the label assignments.

Specific aim A/4 was to evaluate whether the connectivity-based partitions present different diffusion microenvironment. To achieve this, the fractional anisotropy (FA) and mean diffusivity (MD) was provided for clusters in both hemispheres; the calculation was done using the standard equations provided previously. A morphological operation, namely erosion with a 3 * 3 * 3 voxel box kernel was performed on the cluster masks. We assume that this operation reduced the influence of partial volume effect by the adjacent cerebrospinal fluid voxels and therefore the diffusion scalar values can safely be measured in the connectivity-based insular subdomains.

To reveal the anatomical correspondence of the fiber tracts emerging from the newly defined insular subdivisions, we performed probabilistic tractography for each subject, initiated from the voxels representing the discovered insular clusters. As the clustering algorithm was forced to search for two domains, this method provided two different

tractograms for each subject. For each voxel in the brain in each subject, a label was assigned indicating whether that voxel is most likely to be connected to the first cluster (label:1), second cluster (label:2) or no connections to the insula (label:0). Corresponding maps were summed over the subjects and the resulting back-projected tract distributions were visualized (i.e. separately computing maps projected from the 1st and 2nd clusters), in the same way as visualized in the study Menke et al. 2010, Figure 3. [82]. This population-based representation of connectional anatomy of the insula was observed and we described the major connections of the newly defined subdivisions in relation to the territories of widely used digital brain atlases. This visualization step was carried out with the *FSLVIEW* tool (FSL).

3.3.4. Mapping connectivity-based subdomains of the mediodorsal thalamic nucleus

Aim B was to demonstrate the applicability of DTI to study the connectional anatomy of the human thalamus, with special attention to the mediodorsal nucleus. Probabilistic diffusion tractography was performed to trace the interconnections between the human mediodorsal thalamic nucleus and the cerebral cortex. This part of the work flow required special measures to delineate the nucleus.

The masks of the left and right mediodorsal nucleus were drawn in the standard MNI152 neuroimaging space. To define these borders, we used results from a previous work of our collaborators where a mean representation of the human thalamus anatomy was provided by the histological workup of seven thalami [84, 85]; this work is the three-dimensional generalization of the Morel Atlas of the Human Thalamus and Basal Ganglia and therefore contains the depictions of thalamic subdivisions based on cyto- and myeloarchitecture [86]. The idea of using such multi-subject atlases is to incorporate the inter-subject variability of the observed structures. As described in the work by Krauth and co-authors [85], a statistical shape model was constructed that describes this geometrical variability as a multidimensional point cloud, each transformed to a standard stereotactic space, defined by the anterior commissure and posterior commissure landmarks. These data allowed us to use a statistical shape model driven registration method to non-linearly match the outlines of the template's MRI visible thalamus and the corresponding structure from the 3D mean thalamus atlas [87, 88]. Therefore we had access to the borders of the putative borders of the mediodorsal thalamic nucleus in standard space, as defined by the Morel Atlas [86]. This also allowed us to make comparisons with the classical, cytoarchitecture-based

depictions of the anatomy of the mediodorsal nucleus (specific aim B/3.). In the standard space, the 3D outlines of its two subdivisions were accessed (MDmc - magnocellular part and MDpc - parvocellular part).

Similarly to the methodology to characterize the connectivity-based divisions of the insular cortex, we employed the following steps to process DTI data. Estimation of two fiber directions in each image voxel of the brain was carried out by using *BedpostX* (FSL), probabilistic diffusion tractography was initiated from the mask of the mediodorsal thalamic nucleus and probabilistic tractograms were stored in M * N matrices representing the seed voxels (M, rows) and down-sampled brain voxels (N, columns). Cluster analysis by the k-means algorithm was utilized to partition the M seed voxels into two groups that featured the most distinct distribution of connections. Finally, cluster membership labels were mapped back to the reference space for each subject using the inverted spatial transformation of the standardization procedure (specific aim B/2.).

In order to study the spatial distribution of circuits and to localize distant regions connected to the connectivity-based mediodorsal thalamic clusters, a population-based representation of connectional anatomy was required. Probabilistic tractograms for each subject were accessed, and the emerging tract distribution images from the newly defined subdivisions were separated. For each brain voxel, we have assigned a label based on its highest probability of connection to either clusters (separately for left and right hemispheric clusters). Then these labeled maps were correspondingly summed through the 155 subjects. The pattern of this averaged tract anatomy was compared to digital atlas-based gray matter and white matter regions (Harvard-Oxford Cortical Atlas and Juelich Atlas of Fiber Tract Anatomy). Interhemispheric and inter-subject variability was estimated for the volumes of the connectivity-based subdivisions. Their spatial scatter from the group centroid (i.e. the average of coordinates) was determined in the MNI152 space. We have constructed three-dimensional meshes representing the 50th percentile volumes of connectivity-based domains through the examined population, such objects were visually compared to the atlas-based mediodorsal thalamic nuclei borders (specific aim B/3.).

3.3.5. Glioma characterization: general methods

We aimed to use DTI to characterize the spatial patterns of diffusion anisotropy in a pathological scenario, namely in patients with CNS gliomas and correlate such findings with

histological features that are used to type gliomas (aim C). More specifically, to perform analysis based on image features of DTI derived parametric maps, derived from the voxels of the tumor volumes. The final aim therefore is to reveal DTI-based imaging features that can be used noninvasively, preoperatively to predict the WHO grade of CNS gliomas. We also aimed to elucidate whether such DTI-based data are suitable for the creation of a predictive model that would allow determination of the grade of new cases. For this, we describe two main methods: the histogram approach (specific aim C/1) and glioma grade maps (specific aim C/2).

Extracting imaging features for this step was carried out in the space of the diffusion tensor images, no registration or transformation of DTI parametric maps was performed. A crucial step during each procedure was the definition of tumor borders and the delineation of from the brain adjacent to tumor areas (BAT). The extent of the tumors and areas of tumor-associated edema were visually inspected on postcontrast T1-weighted, T2-weighted and FLAIR images. Regions of interests (ROI) were placed in two aspects: the tumor core and tumor periphery. The peripheral region was defined as the maximum high intensity abnormality seen on the unweighted, B_0 images (non-enhancing, T2 abnormality), while the tumor core was outlined inside that region, on the central, low value abnormality seen on fractional anisotropy images. This method is similar to that of Wang et al. where they evaluated the feasibility of using FA and anisotropic diffusion component (q) maps to precisely assess changes in diffusion which are brought about by tumorous infiltration of the white matter [89]. Care was taken to ensure that no regions of cerebrospinal fluid are included inside the tumor borders and also to avoid the inclusion of the peritumoral edema in the analysis. In high grade tumors, the outlined tumor core were identical to the enhancing T1 abnormality while in low grade tumors this comparison was not appropriate due to the low number of enhancing lesions. For the extraction of image features for assessing tumor grade, only the gross tumor core volumes were used, this step followed the inspection of ROIs by a qualified neuroradiologist. Tumor delineation procedure is illustrated in Figure 1.

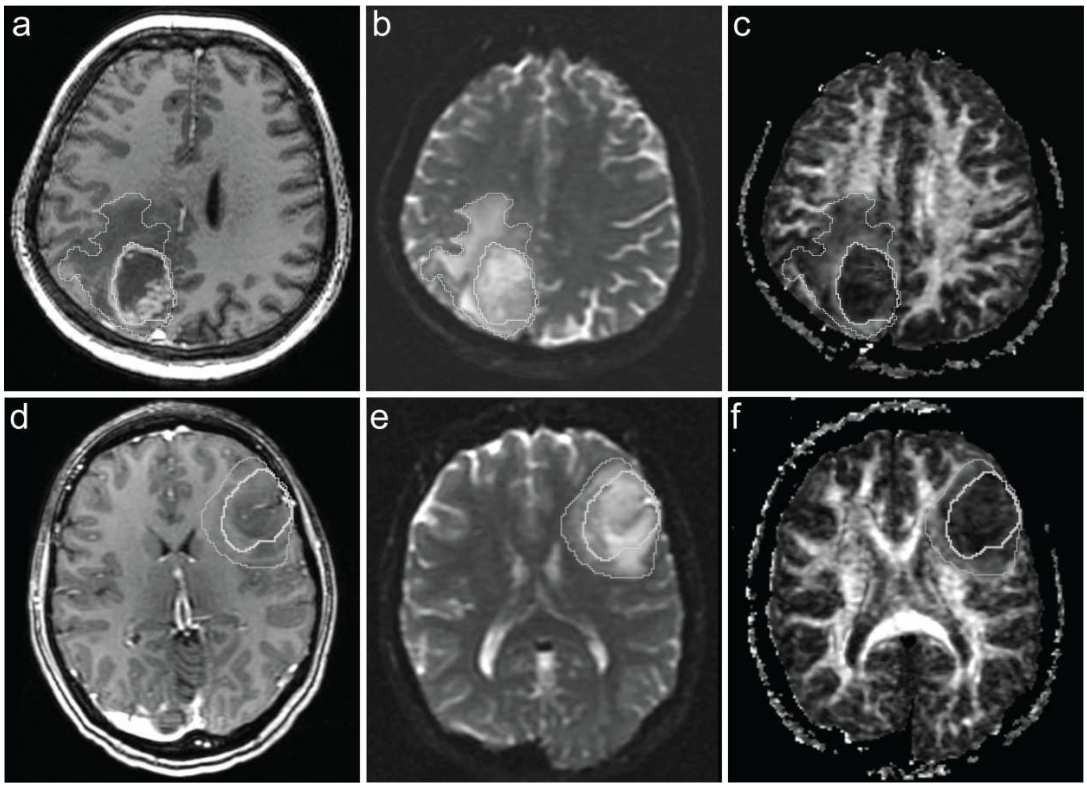

Figure 1. Outlining tumors on B_0 and fractional anisotropy images. First row shows axial images of a patient with GBM while the second row presents a typical case on a non-enhancing low grade glioma. Tumor regions were manually drawn on DTI parametric maps. White border delineates the following two areas: high intensity abnormal region on B_0 images (outside) and low intensity abnormal region on FA maps (inside). (a) and(d): postcontrast T1-weighted; (b), (e): B_0 image; (c), (f): fractional anisotropy map.

3.3.6. Glioma characterization: extracting imaging features as histograms

We hypothesized that the characteristic shape of voxel values' distribution over the entire tumor volume is represented more efficiently as histograms than the classical descriptors of the voxel values' distribution. Compared with the approach of calculating the mean or median values of various DTI-based metrics over the tumor value, individual histogram channels (or bins) could be used as meaningful image features describing the distribution of values. We assume that the pathological attributes which characterizes a WHO grade II or WHO grade IV change the appearance of such histograms in a way that can be revealed with statistical analysis using a supervised learning method.

To support this hypothesis, more conventional statistical parameters of regional diffusion distribution (i.e. means and standard deviations of diffusion tensor metrics: averaged

DWI, FA, longitudinal and parallel diffusivity, trace and B_0) for the whole volume of each tumor were determined. We compared these values in low and high grade glioma groups by using Mann-Whitney-Wilcoxon non-parametric tests.

The steps for determining image features as histograms were the following. Histogram resolution and range was uniformly defined for every image type. The interval between the minimum and maximum pixel values was divided into 25 equally spaced bins. The number of voxels in histogram bins was normalized by the total number of voxels in the sample, and frequency counts were plotted as a function of the bin locations. This allowed storing a normalized histogram for each subject and for each DTI parametric image type. Histogram data were saved and translated into the environment of statistical analysis. For this purpose and for image analysis, a dedicated program code (i.e. macro) was used in the ImageJ software package (National Institutes of Health, USA) [90]. Individual and group-averaged histograms of the tumorous voxel values on DWI, FA, trace, etc. images were generated and visually inspected.

3.3.7. Glioma characterization: statistical evaluations

Specific aim C/1 was to determine if statistical analysis on histogram bins derived from diffusion tensor datasets is capable of classifying gliomas according to their grade. To resolve this classification task, we used multivariate discriminant function analysis (MDA), which was carried out with the SPSS 16.0 for Windows software (SPSS Inc., Chicago, IL, USA).

Multivariate discriminant function analysis, as described by Fisher [91], is a statistical classification method which gives insight into the relationship between group membership and the variables used to predict group membership. During stepwise discriminant analysis, variables (for specific aim C/1: normalized values of histogram channels) are reviewed and evaluated in order to select the ones which contribute most to the discrimination between groups and eventually, a discriminant score is calculated which determines predicted group membership. In our study, 150 variables from the histograms bins of 6 different images (i.e. 6*25 from the following maps: B0, averaged DWI, FA, longitudinal and radial diffusivity, trace) were available. This approach incorporates finding a set of coefficients which, when multiplied by each value in the histogram, gives a score that optimally discriminates between the subgroups under consideration. The resulting model allows prediction of the categorical

variable (i.e. group) of new cases when only the independent variables are known. Further details on MDA can be found in the works by Rippley et al. [92] and Webb et al. [93].

As outlined previously, each case for the aim C was labeled in agreement with the results of a repeated pathological evaluation of WHO grade, this data was used as ground truth for the classifier approach. MDA was employed to classify cases according to their dichotomous group membership (i.e. high grade or low grade glioma). Additionally, classification into 3 categories in accordance with the WHO grades (II-III-IV) was also performed. To evaluate the feasibility of classification on a more homogeneous patient database, analysis was also executed after removing the cases of oligodendroglial components.

We utilized forward stepwise analysis to select the histogram bins that allowed the best classification of the patient dataset. Default vales of the discriminant analysis function in the SPSS software environment were used for this. The success rate of classification was described by two values. First, the classification accuracy was determined with all cases left in, which means *post hoc* prediction of the group membership. We found it necessary to perform *a priori* prediction therefore the validity of the model was assessed by a *leave-one-out cross validation* method. This method estimates the success of classification of each individual case by omitting it from the model and calculating the average rate over the 40 cases, hence yielding a more realistic error rate which might be expected for new observations, i.e., new cases. For more details on the estimation of a classifier performance with cross-validation, see [94]. The discriminating power of the discriminant function (DF) is described by the Wilks' lambda value ranging between zero and 1 (lower values mean higher discriminating power).

3.3.8. Construction of glioma grade maps

Specific aim C/2 was to introduce a new visualization approach that portrays glioma grade by incorporating information from postgadolinium T1- and T2-weighted, diffusion-weighted and parametric images that were computed from diffusion tensor measurements. This would mean the voxel-wise interpretation of imaging features from a multidimensional dataset, where each dimension is a DTI derived parameter or T1 image intensity. The correlation of the multidimensional feature set and a global variable, the class of the tumor (i.e. the grade) is determined by a classifier algorithm. This rationale is similar to the

nosological maps introduced by De Edelenyi et al. [69] or the “oligo-like” and “astro-like” graphical representation of gliomas by Khayal and Nelson [70].

Similarly to the image processing steps for the aim C/1, six DTI derived parametric maps were calculated: T2-weighted images (DWI without diffusion sensitization – B0), directionally averaged raw DWI images, fractional anisotropy, longitudinal and radial diffusivity images, mean diffusivity maps. To obtain anatomical correspondence through the imaging modalities, postcontrast T1 scans were coregistered with the B_0 images (*FLIRT* affine registration algorithm, FSL) and finally, all images were re-sampled to smaller matrices of 128 * 128 voxels. Intensity normalization of the T1-weighted images was performed with the built-in “enhance contrast” command in the ImageJ software tool [90]. Tumor outlines were defined identically to the method described in the section “Glioma characterization: general methods”.

In the next two paragraphs, we describe the steps that were carried out to build a database for the classifier training. The data acquisition and image processing work flow for the specific aim C/2 is summarized in Figure 3. We utilized image information of the 40 patients to generate two different databases for the classifier training procedure. In each database, samples represented consecutive voxels’ values on the images and a categorical variable was also assigned voxel-wise resulting in a total number of 8 variables per voxel. Database “A” provided ground truth for separating the voxels sampled from a low grade tumor or a high grade tumor. In contrast, the aim of database “B” was to separate tumorous regions from non-tumorous regions, as later described, this was only considered important for visualizing the results. Database “A” was built by sampling exclusively the intratumoral regions, the categorical variable was the tumor grade as determined by the histopathology workup (low grade=0; high grade=1) and this was assigned case-wise, without prior spatial control of the histology sampling. Database “B” included every cerebral voxels, whereas the eighth, dichotomous variable described whether the voxel was intratumoral (value: 1) or of normal-appearing brain tissue (value: 0) as determined by the tumor-mask. Database structure is exemplified in Figure 2.

The relationship between imaging data and the categorical variables (i.e. tumor grade, tumor or normal-appearing brain tissue) was analyzed voxel-wise by utilizing a feed-forward, back propagation multilayer perceptron artificial neural network algorithm (ANN) in the SPSS 17.0 for Windows software (SPSS Inc., Chicago, IL, USA). The training regime

wasbased on the random splitting of the dataset into three groups, as offered by the statistical software: training (70% of all voxels), testing (20%) and holdout samples (10%). This supervised learning method resulted in two distinctive models, the first aiming to predict the grade of the glioma while the other assesses if the voxel is sampled from a tumor or from the normal-appearing brain tissue.

After the classifier training, the image dataset was re-evaluated for each patient and outputs were mapped to grayscale images. The voxel-wise outputs of the neural network were continuous variables that estimated the likelihood of voxel group memberships. Grade map generation consisted of the following steps. First, we run the *a priori* trained neural net based on database “A” to generate an image yielding low- and high grade voxel membership probability maps (LGPM and HGPM). The value of this classifier output averaged over the every delineated tumorous voxels is defined as the grade index. As the cut-off value of 0.5 was used for the ANN classifier to distinguish between a low grade or high grade voxel, by the same token, a total tumor grade index below 0.5 would indicate a low grade tumor and 0.5 – 1 values would indicate a high grade tumor. Next, the second neural network estimation – previously trained with database “B” – resulted in an image that quantified the probability of tumor-like regions (tumor probability map, TPM). To provide a graphical representation, LGPM and HGPM images were weighted with the tumor probability maps. Eventually, we defined the glioma grade map as a color-coded composite image where the color lookup table was specified as follows. Blue shade represents low grade regions (LGPM), red shade is for high grade regions (HGPM), the opacity is derived from the TPM, overlaid on the co-registered anatomical T1-weighted image. Resulting images are exemplified in Figure 4.

Patient number	Voxel number	Tumor label	Pathology	T1	B0	DWI	FA	ADC	$\lambda_{\parallel}$	$\lambda_{\perp}$
1	1	0	1	14	65	11	0.234	2.450	1.873	1.153
1	2	1	1	126	1120	234	0.124	1.622	1.556	1.334
	...									
1	442 338	0	1	12	43	9	0.225	2.674	1.664	1.231
2	442 339	1	2	113	325	336	0.351	2.440	1.231	1.119
	...									

Figure 2. Dataset structure for training an artificial neural network classifier. Individual samples are image voxels of 40 subjects, each given a categorical variable: tumor label (e.g. 1 if the voxel was sampled from inside or 0 if outside a tumor), histopathological diagnosis (1: low grade glioma, 2: high grade glioma). Values of 6 imaging features are exemplified.

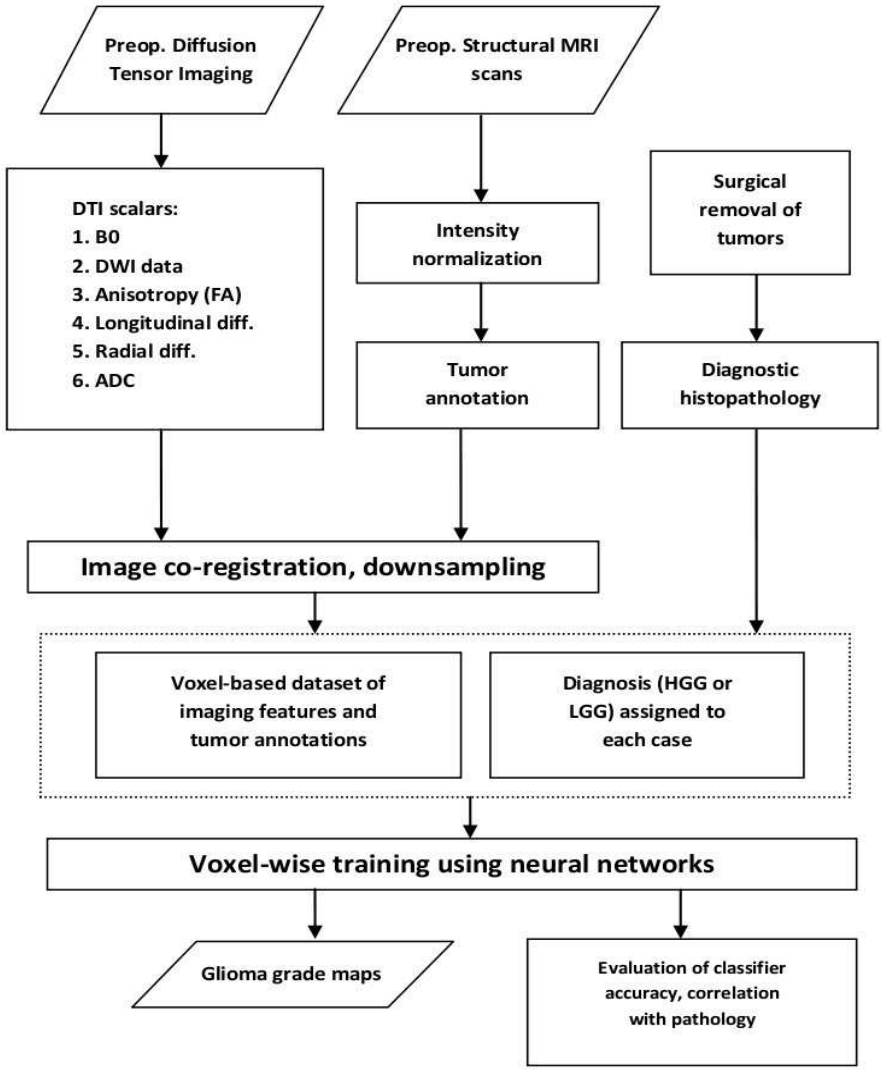

Figure 3. Major data acquisition and image processing steps for specific aim C/2: to develop a graphical representation of the imaging-based interpretation of glioma grade referred to as "gliomas grade maps".

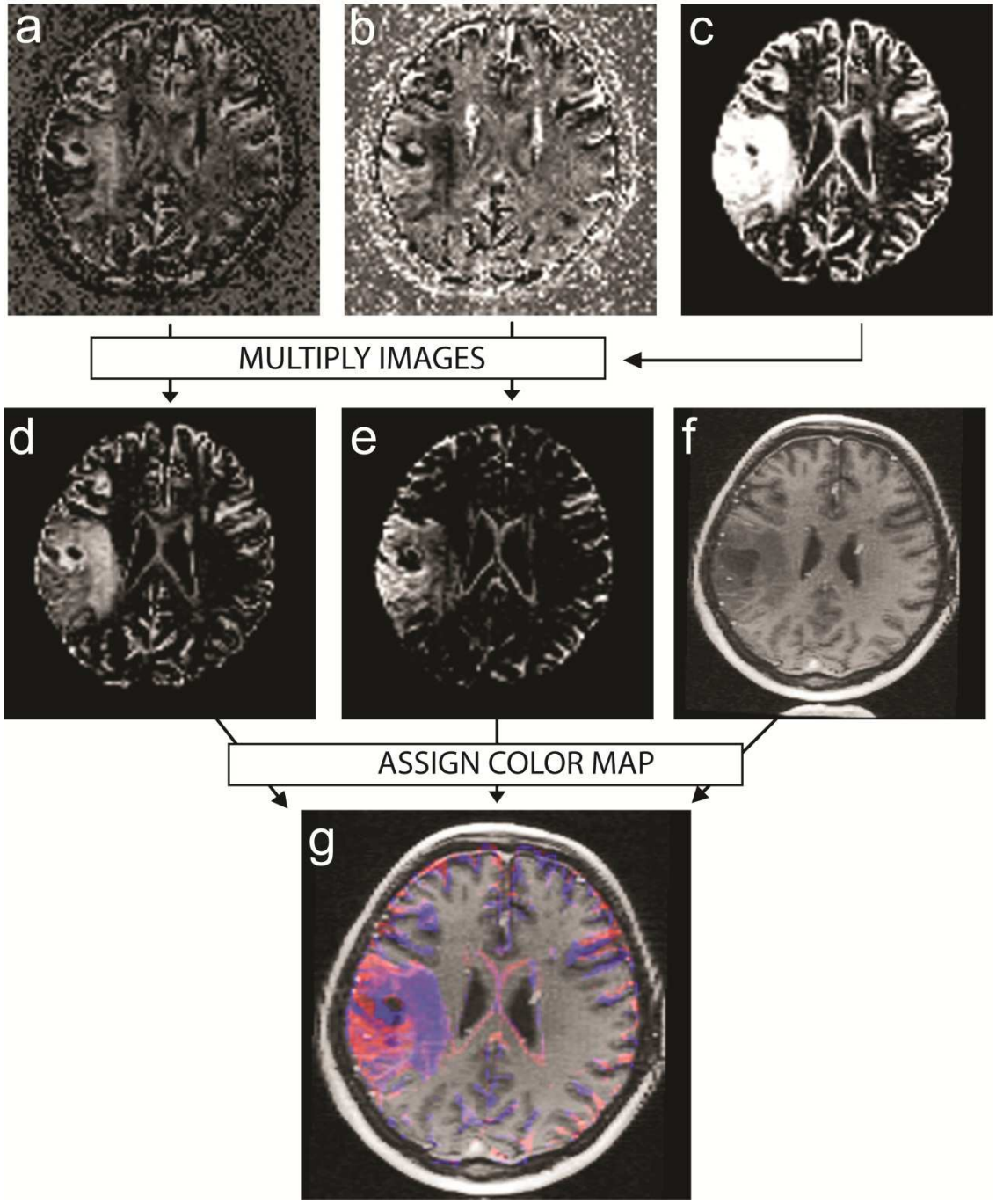

Figure 4. Glioma grade map generation: calculation of intermediate grayscale images and the color-coded glioma grade map (study specific aim C/2). (a) Low grade tumor probability map (LGPM), (b) High grade tumor probability map (HGPM), (c) Tumor probability map (TPM), (d,e) LGPM and HGPM weighted with the TPM, (f) T1-weighted anatomical image. (g) Glioma grade maps are generated by assigning color-code to the probability maps (d,e) and merging them with the postcontrast T1 images.

4. Results

4.1. In vivo description of the connectional anatomy of the insular cortex

Our aim was to use DTI to study the connectional anatomy of the human cerebral cortex, with special focus on the insula. Based on the variability of remote connections, two insular subregions were successfully identified in both hemispheres. The work flow of aim A and illustrations of the probabilistic diffusion tractography procedure is summarized in Figure 5.

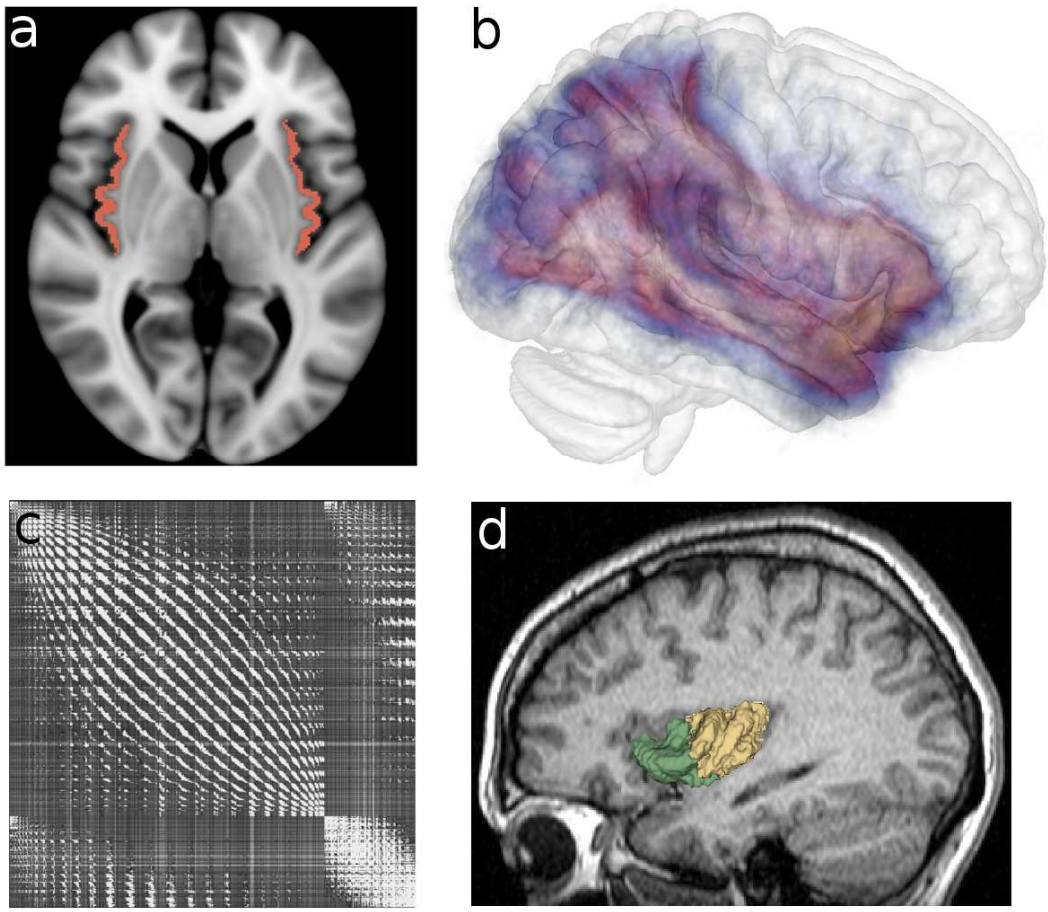

Figure 5. Specific aim A: characterization of connectivity-based subdomains of the insular cortex. (a) Seeding mask of probabilistic diffusion tracing samples in the standard neuroimaging space; (b) 3D visualization of all probabilistic tracing samples emerging from the insular cortex for the study subjects; (c) A reordered cross-correlation matrix for finding connectivity-based clusters in the seed area; elements in the matrix represent the similarities between the seed voxels' remote connections (Page 19.). (d) Back-projected connectivity-based clusters of one subject, overlaid on the native, T1-weighted anatomical image.

The stereotactic coordinates of the COGs of the newly defined insular clusters were consistent, with low deviation from the mean coordinates of each cluster. The spatial scatters from the group center were the following: X axis: 0.36 – 0.49 mm, Y axis:2.27 – 3.88 mm, Z axis: 1.2 – 3.73 mm.

The population-averaged cluster map was controlled for correspondence to major anatomical landmarks (Figure 6.) and also, we compared results with the cytoarchictectonic map of the human insula (Figure 7.). As a result of the connectivity-based subdividing of the insular cortex, we defined an anterior (AI) and posterior insula (PI), the former extending to approximately one-third of the antero-posterior(AP) axis of the insula, delimited by a curved plane perpendicular to the AP axis. In both hemispheres, the AI comprised the limen of the insula and the anterior short gyri enclosed by the precentral insular sulcus and this partition also included the antero-ventral part of the long insular gyri. When comparing the connectivity-based domains with the depiction of cytoarchitectonic subdivisions, we noted a match between the AI and the agranular subdivision plus antero-dorsal dysgranular area was observed. The intersubject variability across the study population (n=40) in terms of cluster volumes is visualized in Figure 8.

In the next three paragraphs, we report the quantitative results of the specific aims A/3 and A/4. The total volume of insular gray matter was not different between the hemispheres. In the left hemisphere, the anterior division of the insular gray matter was found to be significantly larger than the posterior cluster (difference: 34.5%) while on the right side the two partitions were equal in volume. This asymmetry, as expressed by the AI volume to PI volume ratio, showed significant interhemispheric differences.

For each connectivity cluster, the scalar properties of intra-voxel diffusion were determined. The degree of diffusion anisotropy, as expressed by the FA value did not present significant interhemispheric variability and neither was different measured on the AI/PI clusters in the left hemisphere. The FA value of the right AI was significantly higher than the PI. In both hemispheres, the mean diffusivity was consistently and significantly larger in the anterior connectivity partition. Cluster volumes and regional diffusion properties are summarized in Table 4.

Furthermore, we visually controlled the interconnections from each (AI or PI) connectivity-based subdivision. In both hemispheres, tract distributions from the AI revealed

connections with the temporal and occipital lobe, opercular and orbitofrontal cortex, triangular and opercular parts of the inferior frontal gyrus. The density of pathways approaching the orbitofrontal and inferior frontal cortex appeared larger in left hemisphere. The PI subdivision showed extensive connections to the parietal and frontal lobes, predominantly to parts of the somatosensory, motor and premotor cortices adjacent to the midline. An overlap of AI/PI connections in the occipital lobe was noted. Cingular and thalamic connections of each connectivity-based cluster were only observed in a small number of cases. The AI connections were found projecting to the MD nucleus and the PI reaching the ventrolateral thalamus. Images showing the major domains of connections emerging from each insular subdivision are demonstrated in Figure 9.

	Left hemisphere			**Right hemisphere**		
	Anterior cluster	**Posterior cluster**	**AI / PI ratio**	**Anterior cluster**	**Posterior cluster**	**AI / PI ratio**
Volume (mm^3)	**3912** ± 946	**3466** ± 1027	**1.35** ± 0.9	**3560** ± 719	**3848** ± 842	**0.99** ±0.38
(Sig. of antero-posterior volume difference)	**(p=0.047)**			(p=0.104)		
Sig. of left / right volume asymmetry	p=0.065	p=0.073	**p=0.027**			
Fractional anisotropy	**0.181** ± 0.01	**0.178** ± 0.02	**1.02** ±0.09	**0.182** ± 0.02	**0.174** ± 0.01	**1.05** ±0.09
(Sig. of antero-posterior FA difference)	(p=0.382)			**(p=0.01)**		
Mean diffusivity (*10^{-3} mm/s^2)	**1.13** ± 0.1	**0.97** ± 0.06	**1.17** ± 0.14	**1.17** ± 0.15	**0.932** ± 0.05	**1.26** ± 0.16
(Sig. of antero-posterior MD difference)	**(p<0.001)**			**(p<0.001)**		

Table 4. Basic characteristics and measurements of the microstructural properties of water diffusion within the newly defined insular subdivisions, based on their patterns of remote connectivity (study aims A/2 and A/3). Volumes, volume ratios of the connectivity-based insular clusters in the subjects' native space are given. We calculated the regional values of diffusion characteristics: the fractional anisotropy and the mean diffusivity (MEAN ± SD). P values indicate the level of significance of paired, two-sided Student's t-tests.

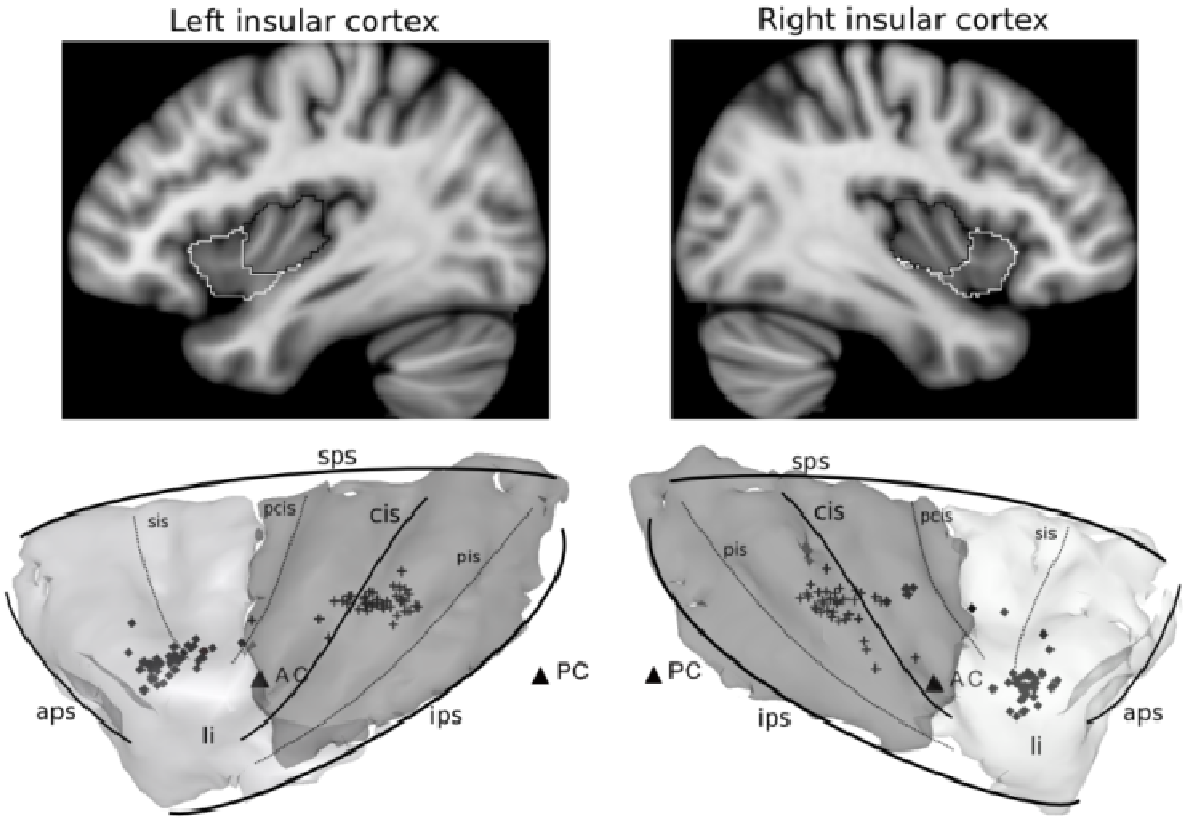

Figure 6. Connectivity-based clusters of the human insular cortex. Top row: sagittal T1-weighted MR image overlaid with the connectivity-based cortical subdivisions averaged through 40 subjects. Black outline: posterior insula (PI), white outline: anterior insula (AI). Bottom row: three-dimensional mesh representing the averaged anterior (white) and posterior insular connectivity clusters, overlay: major insular sulci. Rectangle markers: center-of-gravity points of the AI subdivision of individual subjects in the standard stereotactical space, cross markers: center-of-gravity of the PI subdivision of individual subjects.

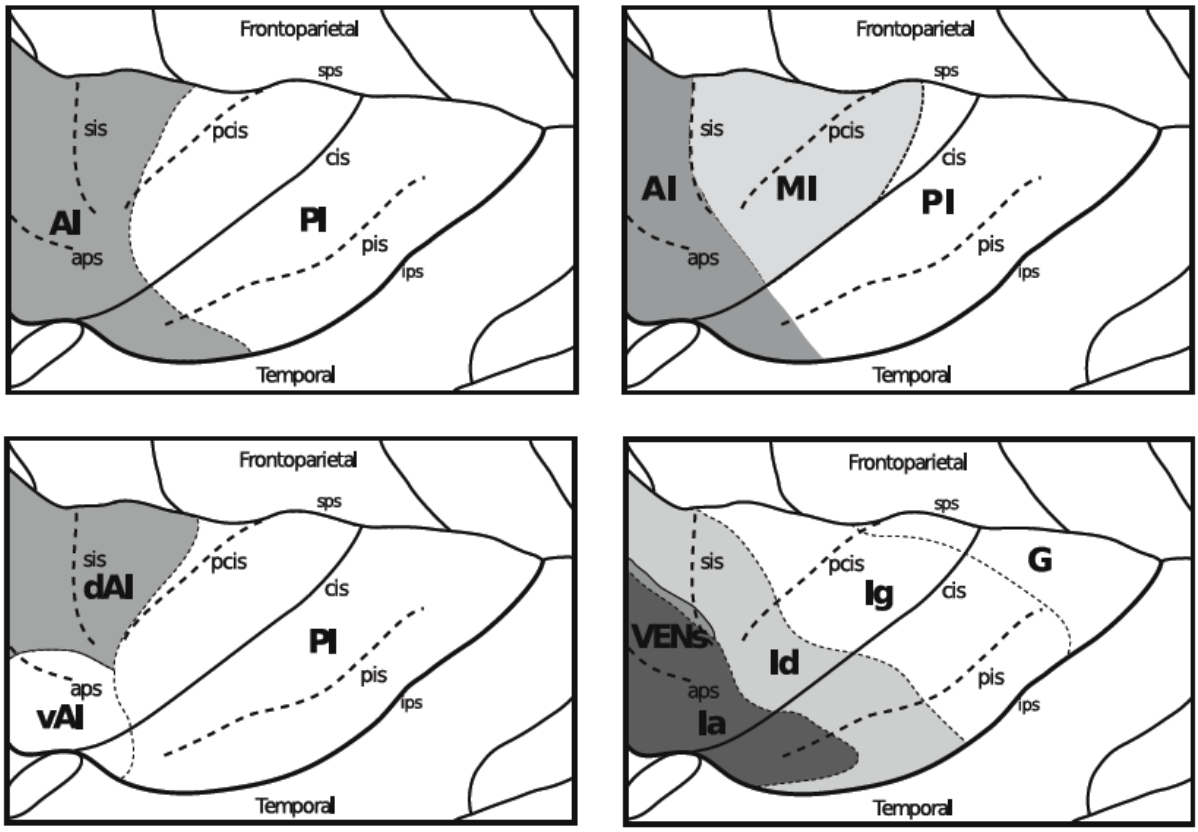

Figure 7. Correspondence between insular anatomy and various subdivision approaches and imaging methods. Top left: clustering based on similarities of structural connectivity (DTI), 2-way clustering. Top right: clustering based on similarities of structural connectivity (DTI), 3-way clustering. Bottom left: three systems of functional connectivity identified using fMRI (schematic drawing based on the paper by Deen et al. 2011). Bottom right: major cytoarchitectural domains of the human insula. aps: anterior periinsular sulcus; sis: short insular sulcus; pcis: precentral insular sulcus; cis: central insular sulcus; pis: postcentral insular sulcus; sps: superior periinsular sulcus; ips: inferior periinsular sulcus; AI, PI: anterior, posterior insula; MI: dorsomedial insula (in 3-way clustering); vAI: ventro-anterior insula; dAI: dorso-anterior insula; Ia: agranular, Id: dysgranular, Ig: granular insula; G: hypergranular subdivision; VENs: von Economo neurons.

Image credits: Bottom right figure is based on unpublished work by Gallay et al. on the cytoarchitectonic map of the human insula (2010 with permission).

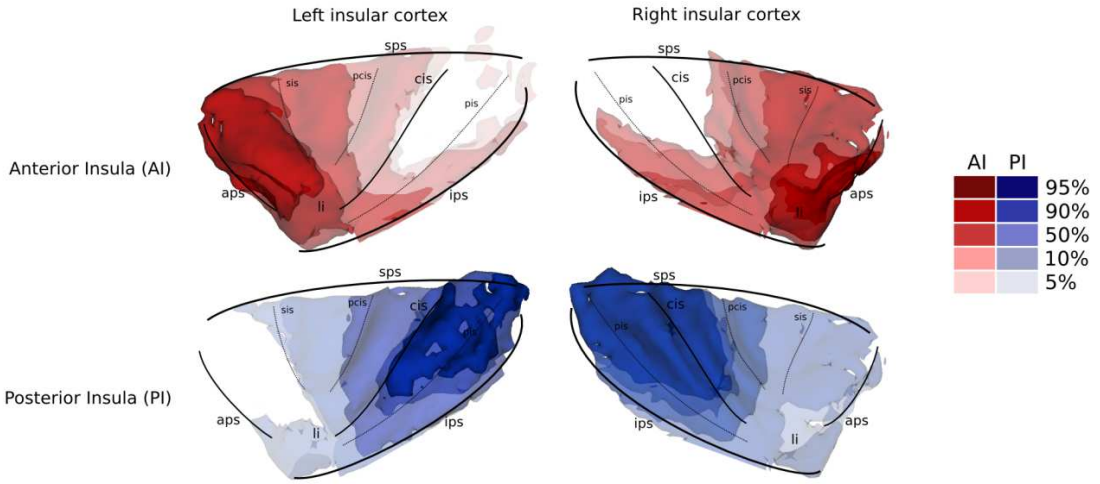

Figure 8. Inter-subject of DTI connectivity-based clustering of the insular cortex. 3D surfaces were generated by accessing the 95th, 90th, 50th, 10th and 5th percentile volumes of each cluster assignment across the population (n=40). Major anatomical landmarks have been illustrated (for description of the nomenclature, see Figure 7.).

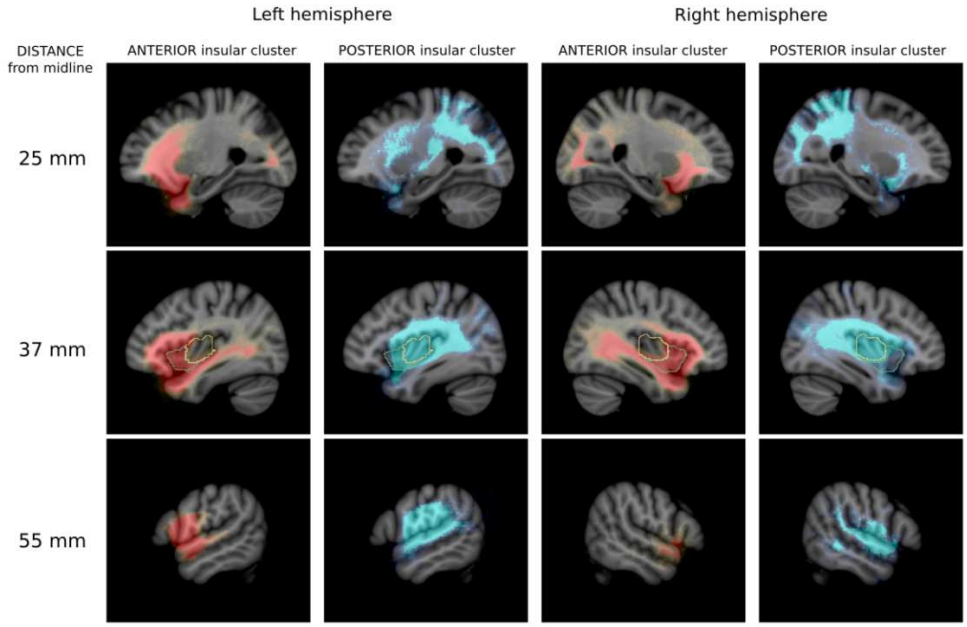

Figure 9. Cross-sectional images demonstrating the fiber tract anatomy of the connectivity-based insular subdivisions (specific aim A/2), overlaid on a standard neuroimaging MRI T1-weighted template (MNI152). Connection probability estimates (n=40, averaged) from the anterior and posterior insular subdivision depicted in three different sagittal images. The distance from the midline in stereotactic space is given.

4.2. In vivo description of the connectional anatomy of the mediodorsal thalamic nucleus

The plane separating the connectivity-based clusters was observed to be parallel to the midline resulting in a medial (MD_{med}) and lateral (MD_{lat}) subdivision of the mediodorsal nucleus. The clusters had a consistently similar shape across subjects, the center-of-gravity (COG) points of the three-dimensional volumes were found to be very similar, the standard deviation of their coordinates were below 1 mm in all axes. The medial domain was significantly larger than the lateral; this difference was on average 36% in both hemispheres. No significant interhemispheric asymmetry was observed for the cluster volumes and the ratios of the medial and lateral segments. Volumetric data are summarized in Table 5. which also includes the reproducibility of connectivity based clustering, marked by the standard deviations of the COG points of each cluster.

	Left hemisphere			**Right hemisphere**		
	MD_{med}	**MD_{lat}**	**med/lat ratio**	**MD_{med}**	**MD_{lat}**	**med/lat ratio**
Volume (mm^3)	**674** ± 98	**535** ± 98	**1.33** ± 0.41	**680** ± 92	**517** ± 92	**1.39** ±0.44
(Sig. of medial-lateral volume difference)	**(p<0.001)**			**(p<0.001)**		
Sig. of left / right volume asymmetry	p=0.535	p=0.051	p=0.174			
Spatial scatter of centroids, X axis (mm)	0.66	0.82		0.69	0.58	
Spatial scatter of centroids, Y axis (mm)	0.53	0.64		0.53	0.46	
Spatial scatter of centroids, Z axis (mm)	0.96	0.98		0.8	0.76	

Table 5. Connectivity-based clusters of the human mediodorsal thalamic nucleus: volumetric measurements and center-of-gravity coordinates. Volumes, volume ratios of the connectivity-based insular clusters are given in the subjects' native space. P values indicate the level of significance of paired, two-sided Student's t-tests.

Next, we controlled the results for the cytoarchitecture-based subdivisions of the mediodorsal nucleus by comparing its borders with the nonlinearly registered thalamus atlas definitions of cytoarchitecture. This investigation revealed only a limited agreement between the average borders of the MD_{med} and the MDmc. The MD_{med} cluster extended approximately to one half of the latero-lateral diameter of the MD nucleus, and unlike the borders of the MDmc, it proportionally extends superiorly and anteriorly. The topography of the MD

connectivity-based clusters and the atlas-based depiction of classical anatomy are visualized in Figure 10.

For each hemisphere, population-based representations of fiber tract anatomy were created. The probabilistic fiber tracking framework allowed following tracts until they reach the cortex, and even further, when the uncertainty of possible trajectories rise. Therefore we were able to review the clusters' connections to atlas-defined cortical and subcortical regions. The MD_{lat} cluster was the source of fibers propagating predominantly into the anterior thalamic radiation and terminating in the superior and middle frontal gyri. The MD_{med} cluster mainly gave rise to pathways that partially joined the inferior fronto-occipital fasciculus and the inferior longitudinal fasciculus, reaching the frontal orbital cortex and various temporal loci. No marked interhemispheric asymmetry was observed for the averaged fiber anatomy. For a more detailed description on interconnections of the MD clusters, see Figure 11.

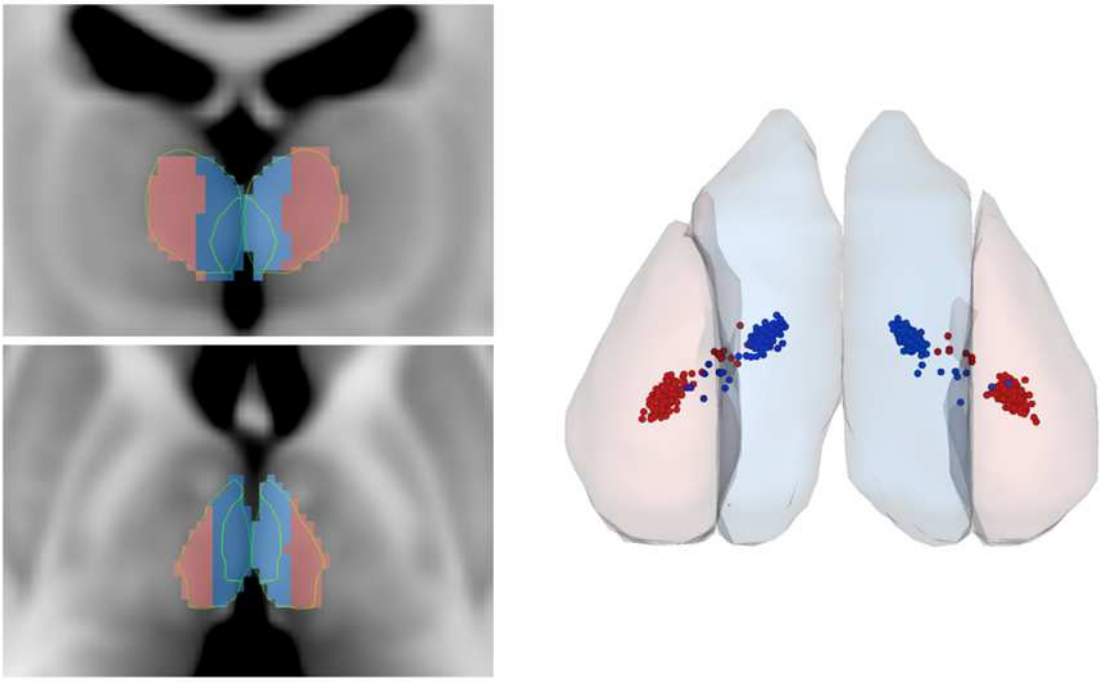

Figure 10. Visualization of the connectivity-based clusters of the human mediodorsal thalamic nucleus. Top and middle image: coronal and axial MRI images of the thalamus, with the connectivity-based clusters overlaid onto the MNI152 T1-weighted template. The outlines of the atlas-basedMDmc and MDpc+pl borders are depicted [86]). Bottom image: 3D representation of the 50th percentile volumes of the medial (MD_{med}) and lateral (MD_{lat}) subdivisions, visualized with the center-of-gravity points of the segments for each subject (n=155).

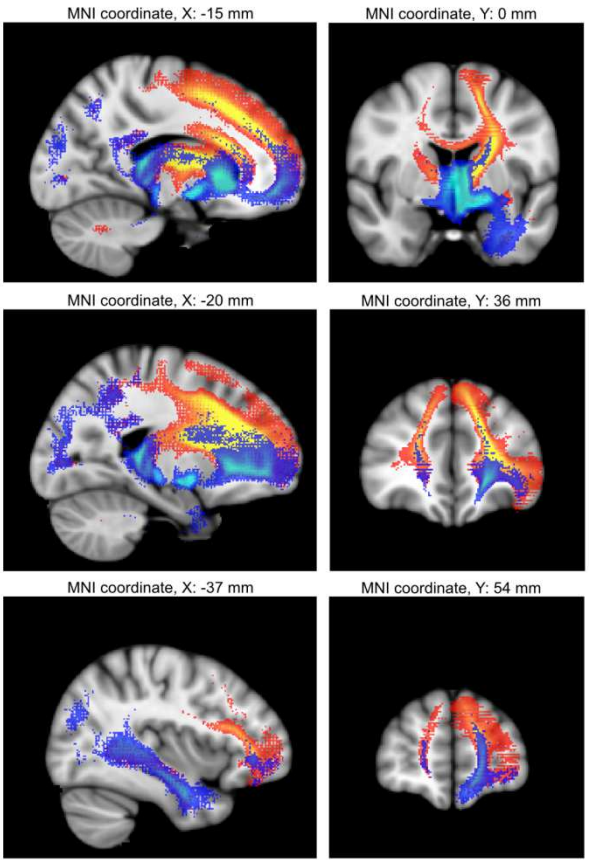

Name of connectivity cluster	Major connections from clusters, GM areas	Major connections from MD clusters, WM areas
Medial cluster	Frontal pole / Brodmann area 10. (orbitobasal parts) Frontal orbital cortex Frontal medial cortex Temporal pole Parahippocampal gyrus, anterior division Amygdala Lateral occipital cortex, superior division	Anterior thalamic radiation Internal capsule, anterior limb Corpus callosum, forceps minor Corpus callosum, genu Inferior fronto-occipital fasciculus, anterior parts Inferior longitudinal fasciculus, anterior parts Uncinate fasciculus
Lateral cluster	Frontal pole / Brodmann area 10. (superior parts) Superior frontal gyrus Middle frontal gyrus, anterior part Inferior frontal gyrus, pars triangularis Supplementary motor cortex	Anterior thalamic radiation Internal capsule, anterior limb Corpus callosum, forceps minor Corpus callosum, genu Corpus callosum, body Inferior fronto-occipital fasciculus, anterior parts External capsule, anterior part

Figure 11. Anatomy of fiber tracts emerging from the connectivity-based subdivisions of the mediodorsal thalamic nucleus (study aim B/2). Averaged representation of the examined population, connection probabilities were overlaid onto the sagittal and coronal cross-sectional images of the MNI152 T1-weighted MR template. Blue overlay: tract trajectories from the MDmc cluster. Red overlay: tract trajectories from the MD_{lat} cluster. We provide a description of connections to gray matter areas (Harvard-Oxford Cortical Atlas and Talairach Daemon nomenclature) and white matter structures (Jüelich Anatomical Fibers Atlas and Talairach Daemon nomenclature).

4.3. Glioma grading by using histogram analysis of diffusion anisotropy

We assumed that the characteristic shape of voxel values' distribution over the entire tumor volume is represented efficiently as histograms and this information can be used to assess the grade of gliomas (study aim C/1). Moreover, we aimed to prove that there is no clear correlation between the mean values of diffusion parameters over the tumor values and the tumor grade. Statistical descriptors of voxel-value distribution in the tumor ROIs were not

significantly different between the groups of high grade (HGG) and low grade gliomas (LGG); however, in high grade cases, a tendency towards higher trace values (HGG: 3.779 ± 0.382, LGG: 3.638 ± 0.485) was discovered. The least significant group difference was observed when values of the directionally averaged DWI images were compared (HGG: 236.1 ± 40.1, LGG: 238.7 ± 35.1). The low significance of differences between groups suggested that classification is not feasible by using ROI analysis over the entire tumor volumes.

We examined LGG and HGG group averaged histograms representing the B_0, FA, DWI, longitudinal and radial diffusivity and trace value distributions in low and high grade gliomas. Groups appeared different, suggesting that classification of individual tumors may be possible. MDA revealed that 6 histogram bins are feasible enough for the discrimination: 3 from the DWI images (value ranges: 100-120; 320-340; 340-360) and single bins from the B0 (value range: 720-800), fractional anisotropy (0.1-0.12) and the longitudinal diffusivity images' histograms (2.2-2.4). Figure 12. exemplifies the differences between the averaged histograms of low-grade (LGG) and high (HGG) grade cases. Results of the MDA evaluation are demonstrated in this image in a way that the histogram bins allowing the most successful classification of glioma subtypes are marked. A discriminant score was calculated by using these bins, and classification was based on these scores.

With all cases left in, the model reached 92.5% precision in classifying cases according to their grade (*post hoc* classification). The "leave-one-out" cross-validation of the same dataset resulted in 87.5% success rate (*a priori* classification), this model resulted in high specificity (88.46%) and high sensitivity (85.71%) in identifying HG gliomas. The low Wilks' lambda value (0.33) and high chi-square score (38.45) indicated good significance in discrimination for this model. Three LG gliomas were incorrectly classified as HG gliomas. One of these tumors was a Gr. II. oligoastrocytoma according to WHO histopathology criteria. It is noteworthy that 65% of the tumor cells of this lesion carried mutant p53 protein. The latter feature is ominous and may suggest imminent progression to a secondary glioblastoma multiforme. No histopathological characteristics seemed to explain the error in the other two cases, both of which were also Gr. II. oligoastrocytomas, unless the samples for histopathology were not representative. Preoperative classification of two glioblastoma multiforme cases was also incorrect as they were identified as LG tumors. Next, we evaluated the discriminant analysis on a slightly modified database: the cases with oligodendroglial components were omitted. This approach resulted in high specificity (100%) with low

sensitivity (72.7%), classification accuracy for both the training and the cross-validation scenario was 87%. Classifying the tumors using the histogram approach, the WHO grade II-III-IV. separation agreed with the grading of the pathologist in 90% of the cases. By means of cross validation, a success rate of 80% was obtained for grouping the cases. Despite the relatively high overall accuracy, we must emphasize that it was not possible to classify the grade III. cases correctly, all the 3 cases were incorrectly categorized either as grade II. or IV.

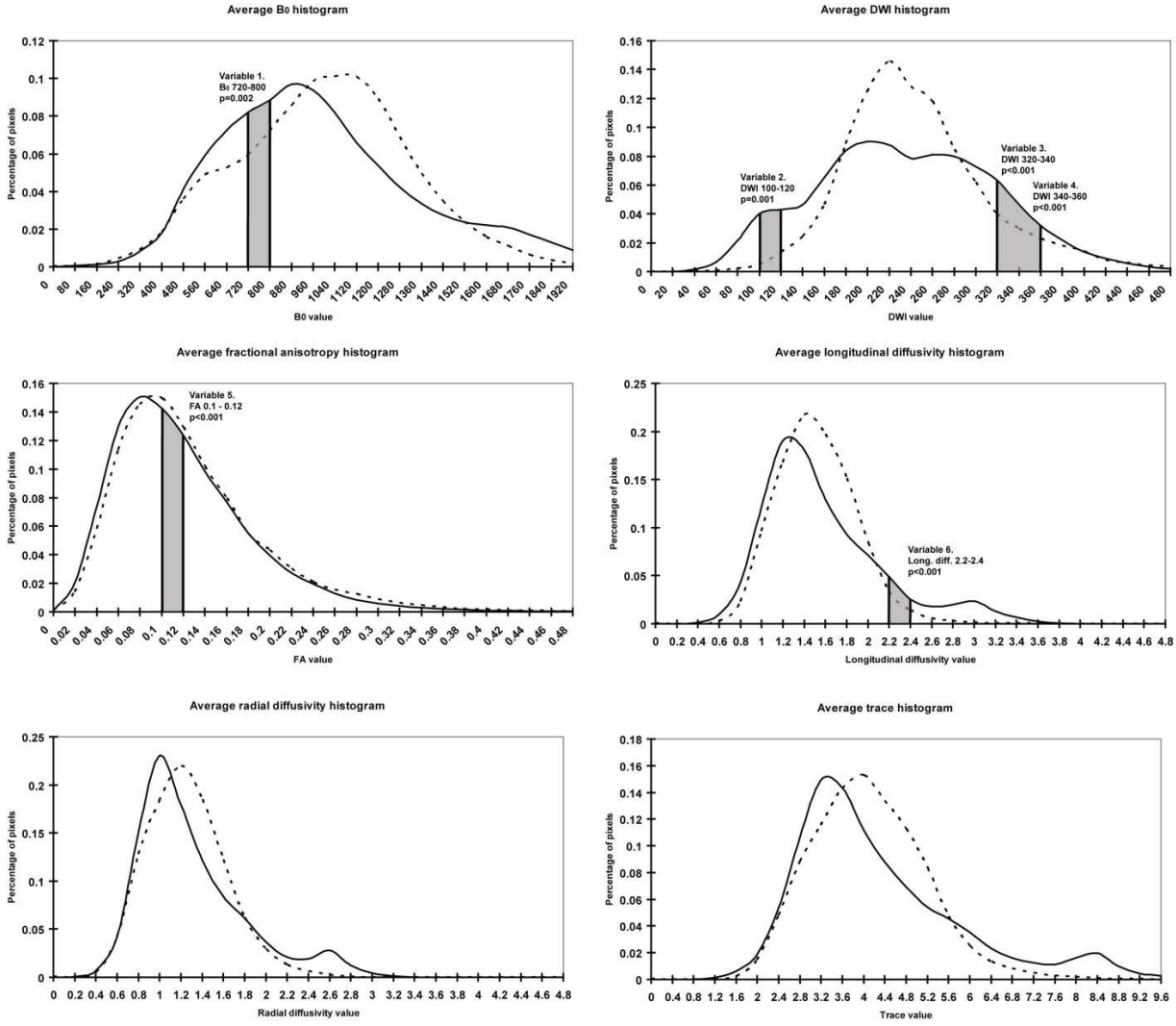

Figure 12. Averaged diffusion-tensor scalar map histograms depicting the differences between low grade (dotted lines) and high grade gliomas (solid lines). Six calculated images were used for the analysis. Although many histograms overlap, there are histogram regions where the percentages of the voxel populations show distinct features. Areas filled with gray represent the range of histogram bins that were selected during the multivariate discriminant analysis in order to precisely discriminate between LG and HG gliomas.

4.4. Characterization of gliomas by grade maps

For the specific aim C/2, we have applied an ANN-based classifier to create parametric maps depicting locally interpreted gliomas grade. This classification was based on a multidimensional dataset consisting of features from the diffusion tensor dataset and T1 weighted images of the subjects. Here we report the voxel-wise precision of these two classifiers in terms of classifying samples (voxels). The first neural network predicted the grade of voxels inside the tumor borders with 82.12 ± 1.84% accuracy (average of 10 runs, tested on the independent holdout sample, putatively marking the accuracy for new observations). Next, the intratumoral voxel membership was estimated correctly in 86.44 ± 0.41% of the samples. Grade index was calculated for each outlined tumor volume. For low grade cases it was 0.281 ± 0.164 (range 0.012 – 0.601) while in high grade lesions it was 0.646 ± 0.148 (range 0.331 – 0.837), the difference was significant ($p<0.001$, Mann-Whitney U test). Additionally, the grade index showed high correlation with the WHO grade (i.e. II, III or IV); Pearson score: 0.709, $p<0.001$. With the cut-off point set to 0.5, the grade index could identify high grade cases with 92.31% specificity, 85.71% sensitivity, AUC: 0.967.

Visual assessment of the TPM (tumor probability map) images, T1 anatomical scans and tumor outline ground truth data revealed good correspondence with the predicted borders, with the following exceptions. Normal-appearing brain regions contained false positive voxels with either blue or red appearance, mainly matching the borders of the gray matter and the cerebrospinal fluid. This error was reported in 8 cases and could presumably be attributed to partial voluming or coregistration artifacts (Figure 13/e, white arrow). Six illustrative images of various glioma subtypes and WHO grades were selected to demonstrate the diagnostic features of grade maps (Figure 13).

The appearance of astrocytoma, oligoastrocytoma grade II and oligodendroglioma grade II tumors on the color-coded grade maps was blue (Figure13/a). Sparse high-grade regions were identified in about six of the 17 non-enhancing and otherwise homogeneous low-grade tumors (Figure13/b) while the focal heterogeneity as marked by contrast-enhancement was revealed correctly in 77.8% (7/9) by regions of red hue in low grade gliomas. WHO grade III (high grade) oligoastrocytomas (Figure13/c) and glioblastoma multiformes predominantly appeared purple to red, with marked heterogeneity as indicated by blue patches (Figure13/d). In 4 of 40 cases, classification by the grade index proved incorrect, for which the following facts are assumed to be responsible. In a patient with a voluminous

glioblastoma multiforme (Figure13/f) this could be putatively ascribed to the relatively high presence of necrotic areas in the tumor, unmasked during the classifier training, hence areas inside necrotic masses were predominantly recognized as low-grade with markedly high-grade rims that closely resembled the contrast-enhancing areas on T1 scans. In the other misclassified high-grade case we found no justification for the result, although the designated grade index was just below the cut-off point. The grade indices for the misclassified glioblastoma multiforme tumors were 0.331 and 0.48, respectively. Two low-grade tumors were improperly classified. In one case the pathologist described high Mib-1 labeling index (20%), hyperchromatic nuclei, geometric neovascularisation and a cellular atypia almost reaching the criteria for grade III classification; further on, closer clinical inspection was suggested for the neuro-oncology team. A cross-section image from the grade map of this case is shown in Figure13/e.

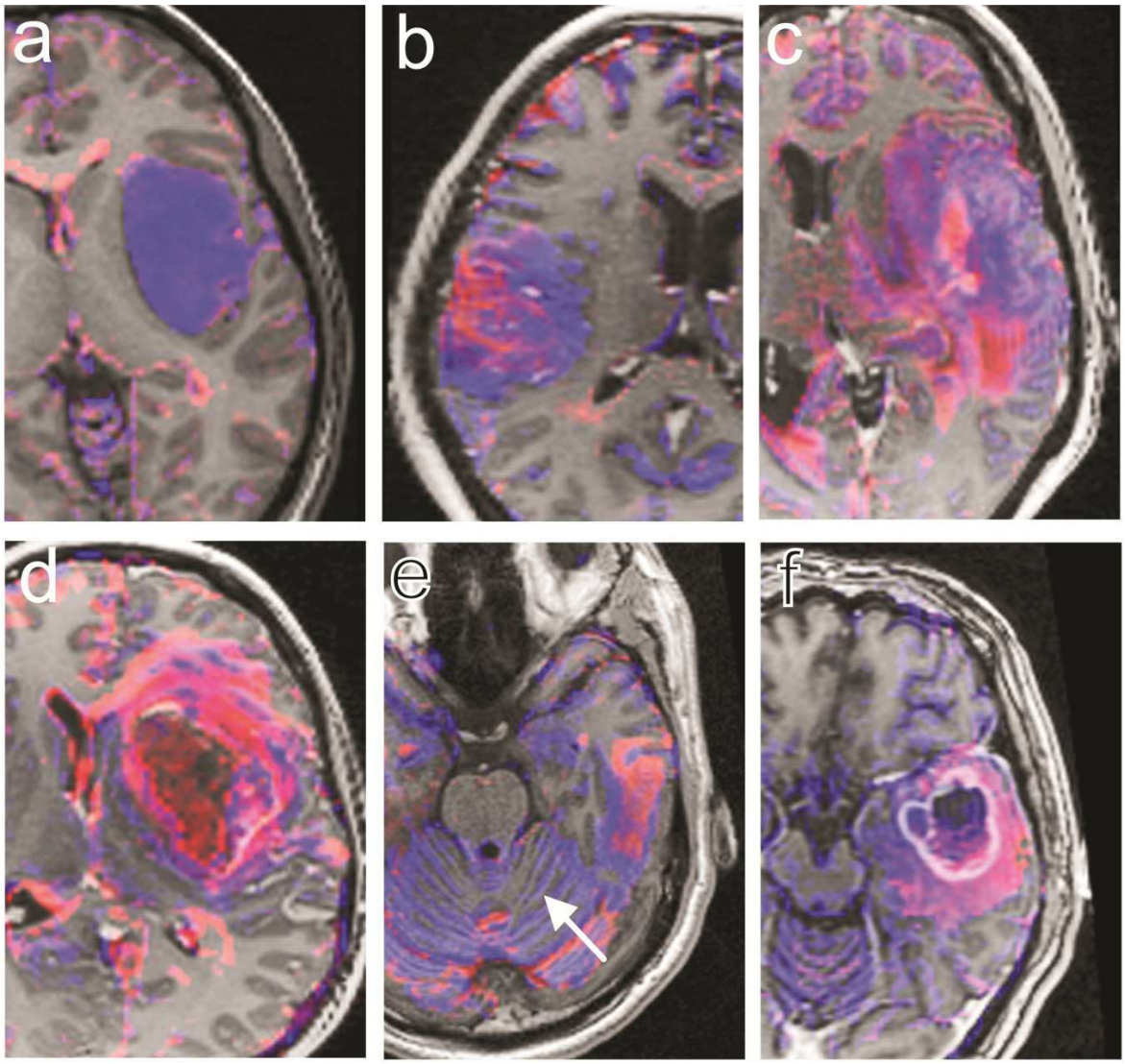

Figure 13. Graphical representation of the imaging-based interpretation of glioma grade (study specific aim C/2). Color-coded glioma grade maps depicting various glioma cases. (a) astrocytoma gr. II. tumors are shown as predominantly blue lesions. (b) oligoastrocytoma gr. II. In a number of cases where the histopathological evaluation judged the lesion as low-grade, the grade maps revealed focal heterogeneity. (c) this astrocytoma gr. III. displays pronounced regional heterogeneity on the glioma grade map; whereas the contrast enhancing regions are well co-localized with the red regions resembling high grade characteristics. (d) Glioblastoma multiforme tumor. (e) a misclassified low-grade case with high cellular atypia. Coregistration and partial volume errors are observed outside the lesion (arrow). (f) glioblastoma multiforme with voluminous necrotic areas, incorrectly classified as low-grade.

5. Discussion

During the last 25 years, diffusion MRI (dMRI) has been widely investigated as a promising modality to image and characterize neurological disorders. dMRI is generally acknowledged as a noninvasive tool to study the white matter organization and microstructure. This rationale gave rise to a new field of research that uses DTI and a new family of image processing techniques to discover brain connectivity and white matter anatomy in living patients and normal subjects [2, 95]. It has been suggested that the subtle changes of diffusion microenvironment can precede macroscopic anatomical alterations and hence diffusion MRI potentially unveils pathological processes in a way that is not accessible with conventional (i.e. T1 or T2 weighted) magnetic resonance imaging [96, 97].

The main focus of our investigation was to use DTI and related image processing methodologies to characterize individual anisotropy patterns of cerebral water diffusion in physiological and pathological scenarios. First, to demonstrate the applicability of DTI in portraying new aspects of the macroscopic anatomy of the human brain, we chose to study the connectional anatomy of the insula and the mediodorsal thalamic nucleus.

5.1. Using DTI to study the connectional anatomy of the insula

Early endeavors to map the human cortex, such as works by K. Brodmann and Von Economo, discovered a limited agreement between macroscopic structures of the brain (gyral or sulcal anatomy) and the organization defined by fine microstructural features like the cytoarchitecture [98, 99]. The same ambiguity is present when attempting to define cortical areas based on similarities in activation patterns when performing executive or cognitive tasks, evidence comes from a large number of neuroimaging studies employing functional MRI. Revitalized by tractography and related techniques, the hodological (i.e. connectionist) approach identifies cortical regions that receive or send out similar connections [100, 79, 81]. Such parcellations potentially generate interest by exploring the human connectional neuroanatomy, nonetheless facilitating the understanding of the cortical representations of major neurocognitive networks.

We used diffusion tractography data to reveal changes in insular connectivity profile by executing a k-means clustering method that labels adjacent areas based on the similarities in the distribution of remote connections. As an initial hypothesis, the algorithms were forced

to search for two segments in the insular gray matter. The impetus for this assumption was that most studies on functional connectivity utilizing resting-state fMRI (r-fMRI) predominantly described a twofold division of the insula into an anteroventral and posterodorsal cluster [24], however, a threefold functional parcellation was also suggested [101]. Parcellating the insula based on diffusion tensor tractography demonstrated a gradual change in tractography patterns with a rostrocaudal trajectory [102].

We conclude that the DTI-based segmentation greatly overlaps with the same depictions of studies using fMRI [24, 101]. It is noteworthy that connections of the ventral part of the long insular gyri and the anterior short insular gyri are similar, this coherence was more pronounced on the structural connectivity segmentations where a larger proportion of the long gyri were included in the area denoted as anterior insula (AI). There is evidence from primates [21-23, 103] and humans that the anterior insula presents a significantly different cytoarchitecture as well as afferent and efferent connectivity than the posterior division. The AI, as defined by its connections, embodied the agranular and part of dysgranular insula which is known to be interconnected to the frontal, orbitofrontal cortex and the amygdaloid body in macaque monkeys [104, 105].

Connectivity data of the human insula is relatively sparse and limited to observations from resting state fMRI measurements or depictions of anatomical connectivity by means of diffusion tensor tractography. A study by Cauda and co-authors [24] concluded that the ventralmost anterior insula is functionally interconnected (i.e., shows temporal correlation of activation patterns) to the rostral anterior cingulate cortex, middle and inferior frontal cortex and the temporoparietal cortex while the dorsal posterior insula is connected to various cortical targets like the dorsal-posterior cingulate, premotor, supplementary motor, temporal and occipital cortex. While tract tracing studies from primates describe complex, region-specific thalamic projections to both the anterior and posterior insula [106], a human fMRI study conflicts with such observations by reporting less pronounced or non-existing posterior insular connection with the thalamus [24]. When controlling the fiber tract anatomy from each connectivity cluster in both hemispheres, we discovered tracts anatomy similar to those of resting state fMRI studies.

Our findings imply that connections of the anterior insula have larger leftward representation relative to the total insular gray matter volume; this leftward dominance of prefrontal and frontal connections coincides with the observations on forebrain asymmetry

[107] or lateralization of prefrontal activations, the latter already described as a biomarker for ingestive behavior [108]. Our result of a larger connectome of the left AI partially conflicts with the observation by Cauda et al., where it was shown that the anterior cluster is rightward dominant. However, this type of interhemispheric dominance is marked by the strength (degree of temporal correlation) of functional and not structural connectivity [24]. In contrast to a previous study using high-resolution MRI scans to assess the structural asymmetries [109], we reported no interhemispheric differences of the overall volume of insular gray matter. It is disputable whether our findings of larger left anterior cluster can be attributed to the structural asymmetry of the AI shown by Watkins et al., as our interpretation of the anterior division was independent of gyral anatomy. Further support for our results on interhemispheric differences comes from a study by Cao et al. [110] which demonstrated a marked L-R asymmetry of anisotropy (i.e. the "orderliness" of diffusion) of the subinsular white matter, implying a putative interhemipsheric asymmetry in the trajectory or density of pathways emerging from or projecting to the insula. The higher mean diffusivity, which is a directionless descriptor of the magnitude of diffusion, hallmarks different water microenvironment in the anterior insula albeit not displaying pronounced interhemispheric variability.

5.2. Using DTI to study the connectional anatomy of the thalamus mediodorsal nucleus

In order to further demonstrate the applicability of DTI to study the connectional anatomy of the human brain, we focused on the mediodorsal thalamic nucleus. As outlined in the study specific aims B/1 – B/3, we aimed to use probabilistic diffusion tractography to trace the interconnections between the human mediodorsal thalamic nucleus and the cerebral cortex. Such data can be used to define connectivity-based subdomains in the mediodorsal nucleus (MD), similarly to our study on the insula. This was done by automatically defining two regions within the MD that presented a coherent and correlated distribution of remote connections. As a continuation of studies attempting to discern the human corticothalamic networks [111, 112, 31], we report the identification of two separated cortico-mediodorsal networks that did not require the subsequent definition of atlas-based cortical targets when performing tractography. This is a major difference compared to the study by Klein et al., where the delineation of the putative dorsolateral prefrontal cortex (DLPFC), lateral orbitofrontal cortex (LOFC) and anterior cingulate cortex (ACC) was necessary. The approach by Klein's workgroup was found feasible to localize subdivisions of the human

mediodorsal nucleus (namely the MDpc, MDfi and caudodorsal MD) based on prior knowledge about cortical projections; moreover, they unveiled remarkable similarities with the macaque brain.

We identified two subdomains in the human mediodorsal nucleus that are separated by a border almost parallel to the sagittal plane: medial part (MD_{med}) and lateral part (MD_{lat}). We controlled the appearance of the connectivity-based subdivisions to the non-linearly matched, histology-based atlas regions. This separation created a medial segment which is similar to the magnocellular part of the mediodorsal nucleus (MDmc), but slightly larger than that and incorporates more than half of the total MD volume. When comparing this observation with earlier tract tracer studies in primates, it was noticeable that such experiments also revealed a sagittally oriented, band-like organization in the MD connectivity patterns [113, 114, 40]. The fiber tracts arising from the connectivity-based segments are in accordance with previous findings using in vivo techniques [112, 31]. The medial band has interconnections with the orbitofrontal cortex and the most rostral parts of the frontal convexities, the frontal pole; while the lateral band is connected to cortical strips that are more superiorly located, e.g. the dorsolateral prefrontal cortex. Klein and colleagues reported a third, cortico-mediodorsal circuit that matched the predictions from macaque: projections from the anterior cingulate cortex (ACC) and the lateral orbitofrontal cortex are separately located in the mediodorsal nucleus, namely in the caudo-dorsolateral parts [115]. Our experiments did not allow separating more than two components of the cortex-mediodorsal thalamus circuitry. Hence it is assumed that the thalamic sector with interconnections to the ACC remained undistinguishable from the MD_{lat} cluster.

We revealed connections between the medial band of the MD (MD_{med}) and three target loci in the temporal lobe: the temporal pole, amygdala and the anterior part of the parahippocampal gyrus. Such connections to the amygdala are in agreement with the findings in Cynomolgus monkeys where predominantly the basal group gave rise to axons connecting to the magnocellular (medial) part of the mediodorsal thalamic nucleus [116]. Classical tract tracing studies in primates confirm the existing connection between the temporopolar cortex and the magnocellular division of the mediodorsal thalamic nucleus [117]. The parahippocampal gyrus was found to be interconnected to both the caudal sector of the MD and the MDmc [118], this only partially overlaps with our observation that the medial band sends connections to the anterior parts of the parahippocampal gyrus. Inputs to the MD from

visually responsive regions were also reported in cats, these were mainly projecting to the anterior and central sectors of the MD [119], such connections were presumably located to the MD_{med} volume in our definition.

Neuroanatomical models describe at least five distinct, segregated frontal-subcortical (i.e., cortico-striato-pallidal-thalamocortical) circuits [46, 120]. It is acknowledged that these networks are organized in parallel but remain partially segregated from each other, especially at subcortical levels. Literature supports our observation that the segregated nature of such networks can be studied by using in vivo probabilistic diffusion tractography or functional MRI and strong correlation can be revealed with previously reported invasive tracing studies [121, 122]. Two segregated networks are known to be involved in motor functioning, originating in the supplementary motor area and the frontal eye fields and mediating somatomotor and oculomotor functions, respectively. Masterman and colleagues emphasized that three of these circuits are particularly mediating aspects of cognition and behavior and the mediodorsal nucleus is accepted as an intermediary relay station for such functions, this role was acknowledged and used as a basis for other works as well [123,124]. These circuits are acknowledged to originate from the DLPFC, orbitofrontal cortex and the ACC. The trajectories of two "cognitive" circuits greatly coincide with the results of the present study suggesting that the two revealed subdivisions might be the thalamic representations of the DLPFC (MD_{lat}) and the orbitofrontal (MD_{med}) segregated networks. This is further supported by the fact that in our study, the algorithms were forced to search for two networks that pass through or originate from the mediodorsal thalamic nucleus and differ from each other with the largest possible degree.

Our approach to study the connectional anatomy of the human thalamus has several limitations. Diffusion tensor imaging and tractography methods were found plausible in recognizing major white matter structures but it is impossible to identify functional connections, individual synapses or tract polarity. Data acquisition is limited to elementary volumes of 4-8 mm3 which is potentially composed of tens of thousands of individual axons that are not necessarily coherent but cross, converge or diverge. Thus the estimation of multiple fiber directions per voxels is necessary, the applied protocol and the relatively high angular resolution of diffusion-weighting (64 directions) allowed us to approximate two of such populations. Furthermore, the definition of gross mediodorsal nucleus borders represents a further possible source of errors. In our case, a mean representation of thalamus geometry

and a non-linear matching method was used that have limited capabilities in tackling with individual variations of fine intrathalamic anatomy. Further studies are required to quantitatively study and validate such of atlas-to-patient registrations.

When studying the connectional anatomy of the insula, the number of diffusion weighting directions (12) allowed estimating one fiber population per voxel, this inherently affects the result of probabilistic tracking of connections. While it is generally acknowledged that brain voxels tend to have multiple fiber directions (e.g. as crossing-fibers), a study on the added-value of multi-orientation models concluded that secondary fibers become less important when performing connectivity-based segmentations; e.g., in the thalamus [125]. The quality of the DTI acquisitions for the specific aim A was also compromised by the anisotropic size of image voxels, i.e. 1.5 * 1.5 * 3.3 mm. We also highlight that to overcome the possible limitations of using a single modality, it would be necessary to conduct confirmatory studies using task based or resting-state fMRI, where the main goal would be to reveal similar subdivision patterns and interactions with psychological measurements.

5.3. Characterization of gliomas by histogram analysis of diffusion anisotropy

Previously in this study, we have shown the applicability of diffusion tensor imaging and mapping of structural connections to study the normal anatomy of the human brain. We further hypothesized that DTI can be used to characterize the spatial patterns of diffusion anisotropy within CNS gliomas and the correlation of such findings with histological features are beneficial in typing (i.e., grading) gliomas.

We aimed this part of our work at the clarification of the interrelationship between the anisotropy patterns of cerebral water diffusion and various grades of gliomas (study aim C). To meet this goal, B_0, directionally averaged DWI, FA, longitudinal, radial diffusivity and mean diffusivity (=trace) were analyzed retrospectively. We discarded the hypothesis that mean voxel values over ROIs might be sufficient enough to assess tumor grade or match any other type of tumor classification. A feature selection from the dataset of individual histogram bins was performed in order to assign a discriminant score (MDA) that allows the best discrimination between tumor classes (grades or histopathological types). Therefore, the MDA score incorporates information from the entire histogram in a way that has been optimized to place the most emphasis on those parts that contribute most to the separation of the groups. A classifier model using 6 histogram variables was feasible enough to delineate

low- and high-grade tumors: evaluating this discriminant function on these particular histogram bins of any new case would yield an estimated tumor grade, the discriminant score was significantly different between the two grade classes ($p<0.001$). Most variables were selected from the DWI histograms. It appears that the heterogeneity among high-grade tumors results in a more deviated and less kurtotic distribution of DWI values while the low-grade cases tend to have modal value of 250 (Figure 12.) and relatively less deviation. The histogram approach revealed that histogram channels far from the peak can discriminate between the two groups. Others reported a correlation between the information obtained from fractional anisotropy of diffusion coefficient images and tumors' grade [126, 127]. According to these reports there exists a correlation between the information obtained from fractional anisotropy of diffusion coefficient images and tumors' grade. Our results contradict this statement since we found no significant differences between mean FA values which characterize different tumor grades. The explanation for the variables selected still remains mathematical; however, it can be concluded that – with the histogram approach – radial diffusivity and trace (ADC*3) maps cannot discriminate between LG and HG tumors when tumors with various tissue compositions are used in the database.

Our observations support the hypothesis that intratumoral heterogeneity can be depicted by calculating histograms for the tumor volume. Clonal selection within tumors is common and is indicated by locally altered diffusion characteristics which result in the modified distribution of voxels' values as indicated by a new peak on the histogram. Such changes do not necessarily affect the mean or median values of the entire voxel population, but significantly change the value of an individual histogram bin.

Preoperative classification of gliomas based on diffusion tensor imaging requires a complex dissection of data. This includes creation of histograms which properly represent individual variations of diffusion values inside the tumors and thus more precise characterization of gliomas becomes possible. This particular statistical approach to tumor classification is superior to those employing single parameters, like employing histogram peak position determination in order to characterize any given histogram. We here quantitatively show that it is more efficient to use MDA of histograms than rely on statistical descriptors (like mean values or standard deviations) of unimodal histograms. The MDA score is adequate for the decision on which group does any individual histogram belong to. Arvinda and colleagues presented a method that employed data from perfusion- and diffusion-

weighted imaging and defined cut-off values for accurate classification [128]. Our results regarding the differentiation of LG and HG gliomas had similar specificity values (Arvinda et al.: 87.1% vs. our 88.4%) while the sensitivity was lower in our approach (Arvinda et al.: 90-95% vs. our 85.7%). In our investigation, the estimation of the classifier performance was defined after leave-one-out cross-validation resulting in an inherently lower specificity and sensitivity compared to the studies that evaluate the discrimination power on the original database.

Important limitations of the present study are the relatively low number of cases (40) on the one hand and the unequal representation of LG and HG cases on the other (13 vs. 27). There is also an ambiguity about the correctness of the pathology workup due to the fact that tissue sampling is not representative for the entire lesion. Even though the radiological workup was prepared to represent the whole tumor volume, the diagnoses used to "train" the database originated from the histopathological findings. We also point out that the discrimination of WHO grade III. cases was insufficient.

Despite all the benefits of multimodal imaging, borders of especially low grade gliomas remain ill-defined and therefore ROI placement is a major cornerstone in the statistical analysis of radiological data. We find it important to minimize the involvement of voxels from non-tumorous areas in the statistical analysis and we suggest the exclusion of displaced or infiltrated WM tracts from the histogram construction; however, eventually measurements of various zones within any given tumor seem inevitable. When delineating HG tumors, the contrast enhancing rims engulfing a necrotic center putatively marks the active part of the tumor, however, this distinction is yet impossible for low grade gliomas. We applied fractional anisotropy images to visualize regions within the tumor where white matter integrity is severely disrupted (i.e. this is hallmarked by low FA values). For such tumors, this region was used as a guidance to outline the three-dimensional volume for the statistical analysis. Similarly, defining the BAT in low grades is not possible unambiguously. We note that the displaced, splayed tracts surrounding the main tumor parts on FA images may indicate relatively spared white matter, but the modality to assess the magnitude of tumorous infiltration is not available yet.

The variations in fractional anisotropy histograms were insignificant between low- and high-grade tumors but the discriminant analysis included an FA bin as well (Figure 12.) consequently highlighting the vulnerability of this unsupervised method for the selection of

features to discriminate between tumor grades. It is highly likely that increasing the number of cases will result in a parallel increase in the reliability of the model therefore it would be desirable to validate the results on a larger set of patients in future studies. The clinical importance of this evolution is obvious: an interdependent evaluation of radiographic (imaging) and morphological (histopathological) data will definitely serve the improvement of therapeutic interventional thinking in glioma patients' proper care.

5.4. Characterization of gliomas by grade maps

The current gold standard for determining glioma subtype and grade is surgical biopsy which is subject to sampling errors. Small volume surgical samples may not represent the entire tumor and due to the marked focal heterogeneity of gliomas it may lead to the false determination of subtype. Valuable radiological features of high-grade gliomas on gadolinium-enhanced MR images are signal intensity heterogeneity, necrosis, hemorrhage, degree of edema and mass effect. To precisely characterize an entity of pronounced heterogeneity like gliomas, further information is required: perfusion studies, MR spectroscopy and diffusion measurements were found feasible for this objective. Such modalities allow calculating functional maps and imaging biomarkers and have been shown to play a complementary role in assessing therapy response or pattern of recurrence [129, 130, 67, 58, 68].

The specific aim C/2 of our study was to develop a graphical representation of the imaging-based interpretation of glioma grade. This was done by correlating the DTI and post gadolinium T1-weighted image derived parameters' in every voxel with the grade of the tumor assigned by a pathologist, and training (optimizing) a neural network-based software classifier to feasibly discriminate every voxel from a low grade and a high grade glioma. Two databases comprising voxel-wise image data of 40 glioma patients were construed whereas artificial neural network computing was utilized to re-classify the original image voxels and by the same token, it becomes possible to classify voxels of undiagnosed cases. Grayscale images were generated that depicted the probabilities of tumor classification (LGPM and HGPM). Eventually, they were combined to produce color-coded composite images, the grade map (Figure 4.). The neural network approach was effective in determining tumor grade of individual voxels whereas a new variable calculated from the voxel-wise outputs of the classifier – the grade index of entire tumor volumes – allowed sufficient classification. In terms of the correct determination of glioma grade, our results exceed the diagnostic power of

conventional MR imaging as described by Law et al. (postgadolinium MRI: 72.5% sensitivity, 65% specificity; grade index classification: 85.7% sensitivity, 92.3% specificity); however, it was reported that the feasibility of using perfusion MRI data vastly improves (95% sensitivity; 57.5% specificity) [61]. Arvinda and co-authors found that ADC, perfusion measurements and their combination could be successfully employed to characterize glioma grade [128]. Herein we report similar results, the grade index being more specific compared to the ADC values alone (92.3% and 87.1%, respectively). While conventional MR imaging provides usable features to discriminate grade IV (GBM) tumors from grade II malignancies, the separation of grade III. anaplastic astrocytomas from low grades is inefficient. White and co-authors described that fractional anisotropy (FA) values and descriptors of the distribution of such values over the tumor volume can increase the sensitivity of grade II. – III. discrimination [131]. Our method provides a novel way to incorporate FA as a feature.

The presented grade map method has several limitations. The reproducibility of the artificial neural network (ANN) algorithm is often disputed; it is generally considered as a "black box" rather than an analytical approach. Increasing the number of processing layers in the ANN will reduce the classification error but consequently causes a loss of generalizability [74]. In our investigation, the number of samples (i.e. voxels) was high and the resulting network structure was kept simple, hence we conclude that the network is not overtrained. It is believed that reproducibility issues would partially be resolved by employing other algorithms such as support vector machines which has already been shown promising in glioma grading [132]. Nevertheless, prospective clinical testing is necessary to evaluate whether a radiologist can perform better with the presented tool than without it. We hypothesized that during the training procedure it is feasible to assign the same categorical diagnosis for each voxel in one particular tumor; however, this presumption required that pathological diagnoses were made from the analyses of representative tissue samples. Matching a specific set of voxels to the position of the surgical sampling would enable better correlation of voxel-wise imaging data and tumor grade. If the assumption is true that the grade index is a quantitative biomarker for depicting alterations in glioma microstructure representative for biological progression, it may also be hypothesized that the values of this biomarker for grade III. tumors are between the values of grade II. and IV. gliomas. Albeit this was not confirmed by our study, the two grade III case had higher grade indices compared to low grade samples: 0.673 ± 0.161 and 0.281 ± 0.164. This unusual distribution of grade indices in grade III. tumors could be attributed to the low number of cases. Another limitation

in our study design is the inclusion of tumors with mixed tissue composition like oligodendrogliomas. It is not evident that the same characteristic changes occur in terms of diffusion or relaxation parameters during the transition from any glioma subtype to higher grades therefore making it harder to generalize this phenomenon.

Szabo De Edelenyi and colleagues found that multidimensional MRI data could be used to create images demonstrating the classification or “nosology” of brain neoplasms; moreover, they suggested incorporating diffusion data in similar future studies [69]. To the best of our knowledge, this is the first study that performs glioma characterization using machine-learning algorithms that combine imaging data of T1- and T2-weighted, diffusion anisotropy and apparent diffusion coefficient information.

5.5 Conclusions

Specific aim A/1. In vivo probabilistic tracking of structural connections using diffusion tensor data provides a novel window on neuroanatomy that was previously unavailable. We used a representative subject population of 40 people to demonstrate the averaged tract anatomy emerging from the human insula. Such fiber tracts were clustered into two distinct populations, originating from the anterior and posterior insula. We provided evidence that the in vivo tract anatomy is similar to the depiction of trajectories by tract tracing studies in primates.

Specific aim A/2. Two subdomains in the human insular cortex were revealed using a k-means approach to cluster the structural connections from this region. We defined them as anterior insula (AI) and posterior insula (PI). Reproducibility across the subject was good, with a marked rostro-caudal variability of the fiber trajectories.

Specific aim A/3. We observed interhemispheric asymmetry in the volumes of connectivity-based subdivisions. This putatively marked a leftward functional dominance of the anterior insula and its reciprocally interconnected targets which influences the size of insular area where similar connections are represented. The mean diffusivity (i.e. magnitude of diffusion) was higher in the anterior insula in both hemispheres while the anisotropy was not different.

Specific aim A/4. The outlines of the change in connectivity profile did not respect the known cytoarchitectural subdivisions and were shown to be independent from the gyral anatomy. Similarly to the literature, we demonstrated a rostro-caudal changing pattern of connectivity domains.

Specific aim B/1. Similarly to the relevant studies in this area, diffusion tractography was plausible to reveal the distribution of thalamocortical (or cortico-thalamic) connectivities. Details about the fiber tract anatomy arising from the mediodorsal thalamic nucleus were provided, which presents a good overlap with the classical descriptions of thalamocortical connections in primates or with other in vivo studies on humans.

Specific aim B/2. Two subdivisions were described within the thalamus mediodorsal nucleus; the areas were defined based on the similarities of the remote connections. The separation border of the connectivity-based clusters was observed to be parallel to the midline resulting

in a medial (MD_{med}) and lateral (MD_{lat}) subdivision of the mediodorsal nucleus, this separation was very reproducible across a population of 155 subjects.

Specific aim B/3. This investigation revealed only a limited agreement between the borders of the connectivity-based subdivisions and the classical, cytoarchitecturally described areas (e.g.: MD_{med} vs. MDmc). The MD_{med} cluster extended approximately to one half of the latero-lateral diameter of the MD nucleus, and unlike the borders of the MDmc, it proportionally extends superiorly and anteriorly.

Specific aim C/1. Constructing histograms of preoperative radiological images over the tumor volume is a feasible technique to extract image features. DTI derived parameters such as values from the B_0, fractional anisotropy, mean diffusivity, etc. images can be incorporated in such a method. When using parametric images from diffusion tensor datasets, this approach allows representation of the grade and enables discrimination of LG and HG gliomas plausibly which has been confirmed by histopathology.

Specific aim C/2. Grade maps are graphical representations of tumor subtype and heterogeneity whilst the grade index was defined as an overall estimate of tumor grade as determined by the assignments of classifiers. In a number of cases, our findings allowed identification of tumors with prominent regional heterogeneity and marked biological progression. The glioma grade map might serve as an imaging biomarker for the characterization of brain gliomas and complement preoperative information available for clinicians.

6. Summary

Water is a fundamental constituent of living creatures and tissue water is structured according to the characteristic features of any given tissue type. A unique property of the brain is that the propagation of water molecules is hindered by microscopic obstacles like the axonal membranes, myelin sheath or the extracellular matrix, resulting in *anisotropic diffusion*. Diffusion tensor magnetic resonance imaging (DTI) provides non-invasive depiction of diffusion through sampling the magnitude and orientation of diffusion anisotropy. Our first study aim was to apply DTI and related image processing techniques to describe normal diffusion anisotropy patterns in the human brain *in vivo*. We assume that such technique can provide information on the connectional topography of different brain areas over large subject groups; we aimed to reveal the distribution of structural connections from the human insular cortex and the mediodorsal nucleus (MD) of the thalamus. Secondly, we focused on the anisotropy patterns of diffusion in pathological conditions, more specifically, to portray the diffusion characteristics in brain neoplasms of glial origin of various WHO grades.

We utilized standard image processing techniques to describe the connectional anatomy of the human insula and the mediodorsal thalamic nucleus. Our explorations included the analysis of 40 and 155 healthy volunteers when studying the normal anisotropy patterns; whereas we used 40 glioma patients for the second aim. Probabilistic DTI tractography was used to map the fiber pathways emerging from the observed areas. Subdomains were mathematically separated that were different in terms of remote interconnections. For the glioma patients, histograms of DTI derived images were fed into a discriminant function analysis based classifier which correlated the features with the histopathologically defined grade.

Fiber tracts were separated into two clusters, originating from the anterior and posterior insula and interhemispheric asymmetry was revealed in such connectivity-based clusters; mean diffusivity values were higher in the anterior insula. We confirmed a rostro-caudal changing pattern of connectivity domains. We provide a description of the two connectivity-based clusters in the MD. Patterns of diffusion anisotropy of preoperative DTI images allowed the prediction of glioma grade with 88.5% specificity and 85.7% sensitivity by using the histogram analysis method.

In vivo probabilistic tracking of structural connections using DTI data provides a novel window on neuroanatomy that was previously unavailable. We provided evidence that the in vivo tract anatomy of the insula and MD is similar to the depiction of trajectories by tract tracing studies in primates. Connectivity-based parcellation of the insular cortex and the mediodorsal thalamic nucleus revealed distinct and separated networks originating from these territories. The characterization of anisotropy patterns in brain gliomas allowed us to construct a classifier model that is feasible for the non-invasive, imaging based preoperative determination of grade.

Összefoglalás

A víz alapvető összetevője az élő szervezeteknek, a víz eloszlása, “strukturáltsága” jellegzetes módon követi az adott szöveti környezet szerkezetét. Az agyszövetek mikroszkopikus felépítése különleges, a vízmolekulák mozgását bizonyos alkotóelemek korlátozzák és a vízdiffúziót *anizotróppá* teszik – ilyen bizonyított struktúrák az axonmembránok, myelinhüvely vagy az extracelluláris mátrix. A diffúziós tenzor mágneses rezonanciás képalkotás (DTI) a diffúziós folyamat non-invazív ábrázolását teszi lehetővé a diffúziós anizotrópia és diffúziós irányok mérésével. Kutatásunk első célja a DTI és képfeldolgozó módszerek alkalmazása volt a normál agyszövetek diffúziós anizotrópia mintázatának feltárására. E technikák segítségével az anatómiai kapcsolatok topográfiája is meghatározható nagyobb esetcsoportokban; a humán insuláris cortex és a thalamus nucleus mediodorsalis (MD) kapcsolatrendszerének jellemzését is célul tűztük ki. Második célunk a diffúziós terek kóros körülmények közötti jellemzése volt, mely célból különböző WHO grádusú agyi glioma DTI adatait elemeztük

A DTI képfeldolgozás és során standard módszereket alkalmaztunk, mellyel a humán insula és MD kapcsolati anatómiája jól leírható *in vivo*. E célok eléréséhez 40 valamint 155 egészséges alany felvételeit használtuk; a gliomákat tartalmazó adatbázisunk 40 beteg képeit tartalmazta. Probabilisztikus DTI traktográfiát alkalmaztunk a vizsgálati területekről eredő rostrendszerek kimutatására; alterületeket különítettünk a távoli kapcsolati mintázatok matematikai elemzésével. A gliomás betegcsoport esetén a DTI-ből származtatható képek hisztogramjainak elemzésével hoztunk létre egy diszkriminancia analízis alapú klasszifikációs modellt, ami ezeket a tulajdonságokat a grádusbecslésre alkalmazza. .

Eredményeink a következők. Az insulából származó rostrendszer alapján anterior és posterior insularis területeket különítettünk el, melyek féltekék közötti méretbeli aszimmetriát mutattak, az anterior insula átlagos diffuzivitás értékei magasabbak voltak a hátulsó területénél. A kapcsolati anatómia rostro-caudalis irányú változását mutattuk ki. A thalamus MD mag két szeparált alterületének konnektivitási anatómiáját leírtuk. A diffúziós mintázatok hisztogram technikával való elemzése a gliomás betegek esetében a szövettanilag meghatározott grádust 88.5%-os specificitással és 85.7% szenzitivitással becsülte.

Az agy strukturális kapcsolatrendszereinek meghatározásában az *in vivo* probabilisztikus DTI traktográfia korábban nem látott lehetőségeket teremt. Az insula és az MD rostrendszerének anatómiájáról gyűjtött eredményeink az állatkísérletes rostkövetéses kutatások eredményeivel jól korrelálnak. A kapcsolatrendszer alapú alterületek kijelölése az insulában és az mediodorsalis thalamusmagban két, egymástól elszeparált kapcsolati hálózatot fedett fel. Az agyi gliomákban mérhető diffúziós anizotrópia mintázatok segítségével olyan módszert mutattunk be, amely nem invazív módon, preoperatív képalkotás segítségével a grádus becslését lehetővé teszi.

References

References cited in the thesis

1. Damadian RV. Apparatus and method for detecting cancer in tissue. U.S. Patent nr.3.789.832.

2. Le Bihan D, Johansen-Berg H. Diffusion MRI at 25: Exploring brain tissue structure and function. Neuroimage 2011; DOI: 10.1016/j.neuroimage.2011.11.006.

3. Dejerine J. Anatomie des Centres Nerveux, pp. 91-198. Rueff et Cie, Paris, 1895.

4. Meynert T. Klinik der Erkrankungen des Vorderhirns, pp. 164-166. Wilhelm Braumüller, Wien, 1884.

5. Cohen N, Weller RO.WHO classification of tumours of the central nervous system (4th edition). Neuropathol Appl Neurobiol 2007; 33:710-711.

6. Ohgaki H, Kleigues P. Population-based studies on incidence, survival rates, and genetic alterations in astrocytic and oligodendroglial gliomas. J Neuropath Exp Neur 2005; 64: 479-489.

7. Stejskal EO. Use of spin echoes in a pulsed magnetic-field gradient to study anisotropic, restricted diffusion and flow. J Chem Phys 1965; 43: 3597–3603.

8. Merboldt K, Hanicke W, Frahm J. Self-diffusion NMR imaging using stimulated echoes. J Magn Reson 1985; 64 : 479–486.

9. Le Bihan D, Breton E, Lallemand D, Grenier P, Cabanis E, Laval-Jeantet M. MR imaging of intravoxel incoherent motions: Application to diffusion and perfusion in neurologic disorders. Radiology 1986; 161:401-407.

10. Beaulieu C. The basis of anisotropic water diffusion in the nervous system? A technical review. NMR Biomed 2002; 15: 435-455.

11. Basser PJ, Pierpaoli C. Microstructural and physiological features of tissues elucidated by quantitative-diffusion-tensor MRI. J Magn Reson, Series B. 1996; 111:209-219.

12. Johansen-Berg H, Rushworth MFS. Using diffusion imaging to study human connectional anatomy. Annu Rev Neurosci 2009; 32: 75-94.

13. Mori S, Crain BJ, Chacko VP, van Zijl PC. Three-dimensional tracking of axonal projections in the brain by magnetic resonance imaging. Ann Neurol 1999; 45:265–269.

14. Jones DK, Simmons A, Williams SC, Horsfield MA. Non-invasive assessment of axonal fiber connectivity in the human brain via diffusion tensor MRI. Magn Reson Med 1999; 42:37–41.

15. Catani M. From hodology to function. Brain 2007; 130: 602-605.

16. Dauguet J, Peled S, Berezovskii V, Delzescaux T, Warfield SK, Born R, et al. Comparison of fiber tracts derived from in-vivo DTI tractography with 3D histological neural tract tracer reconstruction on a macaque brain. Neuroimage 2007; 37: 530-538.

17. Hansen B, Flint JJ, Heon-Lee C, Fey M, Vincent F, King MA, et al. Diffusion tensor microscopy in human nervous tissue with quantitative correlation based on direct histological comparison. Neuroimage 2011; 57: 1458-1465.

18. Behrens TEJ, Woolrich MW, Jenkinson M, Johansen-Berg H, Nunes RG, Clare S, et al. Characterization and propagation of uncertainty in diffusion-weighted MR imaging. Mag Reson Med 2003; 50: 1077-1088.

19. Catani M, Ffytche DH. The rises and falls of disconnection syndromes. Brain 2005; 128:2224-2239.

20. Craig AD. How do you feel? Interoception: the sense of the physiological condition of the body. Nat Rev Neurosci 2002; 3: 655-666.

21. Augustine J. The insular lobe in primates including humans. Neurol Res 1985; 7: 2-10.

22. Augustine JR. Circuitry and functional aspects of the insular lobe in primates including humans. Brain Res Rev 1996; 22: 229-244.

23. Mesulam M, Mufson EJ. Insula of the old world monkey. Architectonics in the insulo-orbito-temporal component of the paralimbic brain. J Comp Neurol 1982; 212: 1-22.

24. Cauda F, D'Agata F, Sacco K, Duca S, Geminiani G, Vercelli A. Functional connectivity of the insula in the resting brain. Neuroimage 2011; 55:8-23.

25. Ziyan U, Westin C. Joint Segmentation of Thalamic Nuclei from a Population of Diffusion Tensor MR Images. In: Székely G (ed). Medical Image Computing and Computer-Assisted Intervention @ MICCAI 2008.Springer Berlin / Heidelberg; 2008. pp. 279-286.

26. Behrens TEJ, Johansen-Berg H, Woolrich MW, Smith SM, Wheeler-Kingshott C, Boulby PA, et al. Non-invasive mapping of connections between human thalamus and cortex using diffusion imaging. Nat Neurosci 2003; 6: 750-757.

27. Johansen-Berg H, Behrens TEJ, Robson MD, Drobnjak I, Rushworth MFS, Brady JM, et al. Changes in connectivity profiles define functionally distinct regions in human medial frontal cortex. P Natl Acad Sci Usa 2004; 101: 13335-13340.

28. Nanetti L, Cerliani L, Gazzola V, Renken R, Keysers C. Group analyses of connectivity-based cortical parcellation using repeated k-means clustering. Neuroimage 2009; 47: 1666-1677.

29. Cerliani L, Thomas RM, Jbabdi S, Siero JCW, Nanetti L, Crippa A, et al. Probabilistic tractography recovers a rostrocaudal trajectory of connectivity variability in the human insular cortex. Hum Brain Mapp 2011; Doi: 10.1002/hbm.21338.

30. Marenco S, Stein JL, Savostyanova AA, Sambataro F, Tan H, Goldman AL, et al. investigation of anatomical thalamo-cortical connectivity and fMRI activation in schizophrenia. Neuropsychopharmacol 2012; 37: 499-507.

31. Klein JC, Rushworth MFS, Behrens TEJ, Mackay CE, de Crespigny AJ, D'Arceuil H, et al. Topography of connections between human prefrontal cortex and mediodorsal thalamus studied with diffusion tractography. Neuroimage 2010; 51: 555-564.

32. Traynor C, Heckemann RA, Hammers A, O'Muircheartaigh J, Crum WR, Barker GJ, et al. Reproducibility of thalamic segmentation based on probabilistic tractography. Neuroimage 2010; 52: 69-85.

33. O'Muircheartaigh J, Vollmar C, Traynor C, Barker GJ, Kumari V, Symms MR, et al. Clustering probabilistic tractograms using independent component analysis applied to the thalamus. Neuroimage 2011; 54: 2020-2032.

34. Pouratian N, Zheng Z, Bari AA, Behnke E, Elias WJ, DeSalles AAF. Multi-institutional evaluation of deep brain stimulation targeting using probabilistic connectivity-based thalamic segmentation. J Neurosurg 2011; 115: 995-1004.

35. Elias WJ, Zheng ZA, Domer P, Quigg M, Pouratian N. Validation of connectivity-based thalamic segmentation with direct electrophysiologic recordings from human sensory thalamus. Neuroimage 2012; 59: 2025-2034.

36. Izquierdo A, Murray EA. Functional interaction of medial mediodorsal thalamic nucleus but not nucleus accumbens with amygdala and orbital prefrontal cortex is essential for adaptive response selection after reinforcer devaluation. J Neurosci 2010; 30: 661-669.

37. Goldman-Rakic PS, Porrino LJ. The primate mediodorsal (MD) nucleus and its projection to the frontal lobe. J Comp Neurol 1985; 242: 535-560.

38. Siwek DF, Pandya DN. Prefrontal projections to the mediodorsal nucleus of the thalamus in the rhesus monkey. J Comp Neurol 1991; 312: 509-524.

39. Negyessy L, Goldman-Rakic P. Morphometric characterization of synapses in the primate prefrontal cortex formed by afferents from the mediodorsal thalamic nucleus. Exp Brain Res 2005; 164: 148-154.

40. Ray JP, Price JL. The organization of projections from the mediodorsal nucleus of the thalamus to orbital and medial prefrontal cortex in macaque monkeys. J Comp Neurol 1993; 337: 1-31.

41. Öngür D, Price JL. The organization of networks within the orbital and medial prefrontal cortex of rats, monkeys and humans. Cereb Cortex 2000; 10: 206-219.

42. Erickson SL, Lewis DA. Cortical connections of the lateral mediodorsal thalamus in cynomolgus monkeys. J Comp Neurol 2004; 473: 107-127.

43. Van der Werf YD, Witter MP, Uylings HBM, Jolles J. Neuropsychology of infarctions in the thalamus: a review. Neuropsychologia 2000; 38: 613-627.

44. Van der Werf YD, Scheltens P, Lindeboom J, Witter MP, Uylings HBM, Jolles J. Deficits of memory, executive functioning and attention following infarction in the thalamus; a study of 22 cases with localised lesions. Neuropsychologia 2003; 41: 1330-1344.

45. Pulsipher DT, Seidenberg M, Guidotti L, Tuchscherer VN, Morton J, Sheth RD, et al. Thalamofrontal circuitry and executive dysfunction in recent-onset juvenile myoclonic epilepsy. Epilepsia 2009; 50: 1210-1219.

46. Alexander GE, DeLong MR, Strick PL. Parallel Organization of Functionally Segregated Circuits Linking Basal Ganglia and Cortex. Annu Rev Neurosci 1986; 9: 357-381.

47. Luders E, Narr KL, Thompson PM, Toga AW. Neuroanatomical correlates of intelligence. Intelligence 2009; 37: 156-163.

48. Haier RJ, Jung RE, Yeo RA, Head K, Alkire MT. Structural brain variation and general intelligence. Neuroimage 2004; 23: 425-433.

49. Sinha S, Bastin ME, Whittle IR, Wardlaw JM. Diffusion tensor MR imaging of high-grade cerebral gliomas. Am J Neuroradiol 2002; 23:520-527.

50. Tropine A, Vucurevic G, Delani P, Boor S, Hopf N, Bohl J, et al. Contribution of diffusion tensor imaging to delineation of gliomas and glioblastomas. J Magn Reson Imaging 2004; 20: 905-912.

51. Kono K, Inoue Y, Nakayama K, Shakudo M, Morino M, Ohata K, et al. The role of diffusion-weighted imaging in patients with brain tumors. Am J Neuroradiol 2001; 22: 1081-1088.

52. Sugahara T, Korogi Y, Kochi M, Ikushima I, Shigematu Y, Hirai T, et al. Usefulness of diffusion-weighted MRI with echo-planar technique in the evaluation of cellularity in gliomas. J Magn Reson Imaging 1999; 9: 53-60.

53. Zimmerman RD. Is There a Role for Diffusion-weighted imaging in patients with brain tumors or is the "Bloom off the Rose"? Am J Neuroradiol 2001; 22: 1013-1019.

54. Khayal IS, McKnight TR, McGue C, Vandenberg S, Lamborn KR, Chang SM, et al. Apparent diffusion coefficient and fractional anisotropy of newly diagnosed grade II gliomas. NMR Biomed 2009; 22: 449-455.

55. Inoue T, Ogasawara K, Beppu T, Ogawa A, Kabasawa H. Diffusion tensor imaging for preoperative evaluation of tumor grade in gliomas. Clin Neurol Neurosurg 2005; 107: 174-180.

56. Goebell E, Paustenbach S, Vaeterlein O, Ding X, Heese O, Fiehler J, et al. Low-grade and anaplastic gliomas: differences in architecture evaluated with diffusion-tensor MR imaging. Radiology 2006; 239: 217-222.

57. Murakami R, Hirai T, Sugahara T, Fukuoka H, Toya R, Nishimura S, et al. Grading astrocytic tumors by using apparent diffusion coefficient parameters: superiority of a one- versus two-parameter pilot method. Radiology 2009; 251: 838-845.

58. Verma R, Zacharaki EI, Ou Y, Cai H, Chawla S, Lee S, et al. Multiparametric tissue characterization of brain neoplasms and their recurrence using pattern classification of MR images. Acad Radiol 2008; 15: 966-977.

59. Emblem KE, Scheie D, Due-Tonnessen P, Nedregaard B, Nome T, Hald JK, et al. Histogram Analysis of MR Imaging-Derived Cerebral Blood Volume Maps: Combined glioma grading and identification of low-grade oligodendroglial subtypes. Am J Neuroradiol 2008; 29: 1664-1670.

60. Tozer DJ, Jäger HR, Danchaivijitr N, Benton CE, Tofts PS, Rees JH, et al. Apparent diffusion coefficient histograms may predict low-grade glioma subtype. NMR Biomed 2007; 20: 49-57.

61. Law M, Yang S, Wang H, Babb JS, Johnson G, Cha S, et al. Glioma grading: sensitivity, specificity, and predictive values of perfusion MR imaging and proton MR spectroscopic imaging compared with conventional MR imaging. Am J Neuroradiol 2003; 24: 1989-1998.

62. Law M, Young R, Babb J, Pollack E, Johnson G. Histogram analysis versus region of interest analysis of dynamic susceptibility contrast perfusion MR imaging data in the grading of cerebral gliomas. Am J Neuroradiol 2007; 28: 761-766.

63. Dehmeshki J, Ruto AC, Arridge S, Silver NC, Miller DH, Tofts PS. Analysis of MTR histograms in multiple sclerosis using principal components and multiple discriminant analysis. Magn Reson Med 2001; 46: 600-609.

64. Dehmeshki J, Van Buchem MA, Bosma GPT, Huizinga TWJ, Tofts PS. Systemic lupus erythematosus: diagnostic application of magnetization transfer ratio histograms in patients with neuropsychiatric symptoms - initial results. Radiology 2002; 222: 722-728.

65. Calvar JA, Meli FJ, Romero C, Yenez ML, Calcagno P, Martinez AR, Lambre H, et al. Characterization of brain tumors by MRS, DWI and Ki-67 labeling index. J Neurooncol 2005; 72: 273-280.

66. Higano S, Yun X, Kumabe T, Watanabe M, Mugikura S, Umetsu A, et al. Malignant astrocytic tumors: clinical importance of apparent diffusion coefficient in prediction of grade and prognosis. Radiology 2006; 241: 839-846.

67. Mardor Y, Roth Y, Ocherashvilli A, Spiegelmann R, Tichler T, Daniels D, et al. Pretreatment prediction of brain tumors' response to radiation therapy using high b-value diffusion-weighted MRI. Neoplasia 2004; 6: 136-142.

68. Pope WB, Kim HJ, Huo J, Alger J, Brown MS, Gjertson D, et al. Recurrent glioblastoma multiforme: ADC histogram analysis predicts response to Bevacizumab treatment. Radiology 2009; 252: 182-189.

69. De Edelenyi FS, Rubin C, Esteve F, Grand S, Decorps M, Lefournier V, et al. A new approach for analyzing proton magnetic resonance spectroscopic images of brain tumors: nosologic images. Nat Med 2000; 6: 1287-1289.

70. Khayal IS, Nelson SJ. Characterization of low-grade gliomas using RGB color maps derived from ADC histograms. J Magn Reson Imaging 2009; 30: 209-213.

71. Luts J, Laudadio T, Idema AJ, Simonetti AW, Heerschap A, Vandermeulen D, et al. Nosologic imaging of the brain: segmentation and classification using MRI and MRSI. NMR Biomed 2009; 22: 374-390.

72. Carano RAD, Ross AL, Ross J, Williams SP, Koeppen H, Schwall RH, et al. Quantification of tumor tissue populations by multispectral analysis. Magn Reson Med 2004; 51: 542-551.

73. Baxt WG. Application of artificial neural networks to clinical medicine. Lancet 1995; 346: 1135-1138.

74. Hagberg G. From magnetic resonance spectroscopy to classification of tumors. A review of pattern recognition methods. NMR Biomed 1998; 11: 148-156.

75. Wang X, Yang J, Jensen R, Liu X. Rough set feature selection and rule induction for prediction of malignancy degree in brain glioma. Comput Methods Programs Biomed 2006; 83: 147-156.

76. Joshi DM, Rana NK, Misra VM. Classification of brain cancer using artificial neural network. Electronic Computer Technology (ICECT), 2010 International Conference on 2010; 112-116.

77. Castellanos FX, Leventhal B, Milham M. Nathan Kline Institute (NKI) / Rockland Sample. http://fcon_1000.projects.nitrc.org/indi/pro/nki.html Accessed 01 July 2011

78. Smith SM., Jenkinson M, Woolrich MW, Beckmann CF, Behrens TEJ, Johansen-Berg H et al. Advances in functional and structural MR image analysis and implementation as FSL. NeuroImage 2004;23(Suppl 1):S208-S219.

79. Klein JC, Behrens TEJ, Robson MD, Mackay CE, Higham DJ, Johansen-Berg H. Connectivity-based parcellation of human cortex using diffusion MRI: Establishing reproducibility, validity and observer independence in BA 44/45 and SMA/pre-SMA. Neuroimage 2007; 34:204-211.

80. Tomassini V, Jbabdi S, Klein JC, Behrens TEJ, Pozzilli C, Matthews PM, et al. Diffusion-weighted imaging tractography-based parcellation of the human lateral premotor cortex identifies dorsal and ventral subregions with anatomical and functional specializations. J Neurosci 2007; 27: 10259-10269.

81. Jbabdi S, Woolrich MW, Behrens TEJ. Multiple-subjects connectivity-based parcellation using hierarchical Dirichlet process mixture models. Neuroimage 2009; 44: 373-384.

82. Menke RA, Jbabdi S, Miller KL, Matthews PM, Zarei M. Connectivity-based segmentation of the substantia nigra in human and its implications in Parkinson's disease. Neuroimage 2010; 52: 1175-1180.

83. JakabA, Molnar P, Bogner P, Beres M, Berenyi E. Connectivity-based parcellation reveals interhemispheric differences in the insula. Brain Topogr 2011; DOI: 10.1007/s10548-011-0205-y.

84. Niemann K, Mennicken VR, Jeanmonod D, Morel A. The Morel stereotactic atlas of the human thalamus: atlas-to-MR registration of internally consistent canonical model. Neuroimage 2000; 12: 601-616.

85. Krauth A, Blanc R, Poveda A, Jeanmonod D, Morel A, Székely G. A mean three-dimensional atlas of the human thalamus: Generation from multiple histological data. Neuroimage 2010; 49: 2053-2062.

86. Morel A. Stereotactic Atlas of the Human Thalamus and Basal Ganglia. New York: Informa Healthcare USA, inc., 2007.

87. Rao A, Aljabar P, Rueckert D. Hierarchical statistical shape analysis and prediction of sub-cortical brain structures. Med Image Anal 2008; 12: 55-68.

88. Jakab A, Blanc R, Morel A, Berenyi E, Szekely G. Connectivity-augmented surgical targeting: individualization of a mean three-dimensional atlas of the human thalamus.“Proceedings of the European Society of Neuroradiology (ESNR) Congress” in Neuroradiology 2011; 53(Supplement 1): 1-2.

89. Wang W, Steward CE, Desmond PM. Diffusion Tensor Imaging in Glioblastoma Multiforme and Brain Metastases: The Role of p, q, L, and Fractional Anisotropy. Am J Neuroradiol 2009; 30: 203-208.

90. Abramoff MD, Magelhaes PJ, Ram SJ. Image Processing with ImageJ. Biophotonics International 2004; 11:36-42.

91. Fisher RA. The use of multiple measurements in taxonomic problems. Annals Eugenics 1936; 7: 179-188.

92. Ripley BD. Pattern recognition and neural networks. Cambridge University Press, Cambridge 1997, page 91.

93. Webb A. Statistical pattern recognition. Oxford University Press. New York 1999, page 6.

94. Fukunaga K, Hayes R. Estimation of classifier performance. IEEE Trans Pattern Anal Machine Intel 1989; 11:1087-1097.

95. Assaf Y, Pasternak O. Diffusion tensor imaging (DTI)-based white matter mapping in brain research: a review. J Mol Neurosci 2008; 34: 51-61.

96. Horsfield MA, Jones DK. Applications of diffusion-weighted and diffusion tensor MRI to white matter diseases? A review. NMR Biomed 2002; 15: 570-577.

97. Sundgren PC, Dong Q, Gomez-Hassan D, Mukherji SK, Maly P, Welsh R. Diffusion tensor imaging of the brain: review of clinical applications. Neuroradiology 2004; 46: 339-350.

98. Brodmann K. Vergleichende Lokalisationslehre der Großhirnrinde, in ihren Prinzipien dargestellt auf Grund des Zellenbaues, Johann Ambrosius Barth, Leipzig, 1909, pp. 285-321,

99. Economo C, Koskinas GN. Die Cytoarchitektonik der Hirnrinde des erwachsenen Menschen. Springer Verlag, Wien, 1925.

100. Johansen-Berg H, Behrens TEJ, Robson MD, Drobnjak I, Rushworth MFS, Brady JM, et al. Changes in connectivity profiles define functionally distinct regions in human medial frontal cortex. P Natl Acad Sci Usa 2004; 101:13335-13340.

101. Deen B, Pitskel NB, Pelphrey KA. Three systems of insular functional connectivity identified with cluster analysis. Cerebral Cortex 2011; 21: 1498-1506.

102. Cerliani L, Thomas RM, Jbabdi S, Siero JCW, Nanetti L, Crippa A, et al. Probabilistic tractography recovers a rostrocaudal trajectory of connectivity variability in the human insular cortex. Hum Brain Mapp 2011; Doi: 10.1002/hbm.21338.

103. Gallay DS, Gallay MN, Jeanmonod D, Rouiller EM, Morel A. The insula of Reil revisited: multiarchitectonic organization in macaque monkeys. Cereb Cortex 2012; 22: 175-190.

104. Carmichael ST, Price JL. Architectonic subdivision of the orbital and medial prefrontal cortex in the macaque monkey. J Comp Neurol 1994; 346: 366-402.

105. Stefanacci L, Amaral DG. Topographic organization of cortical inputs to the lateral nucleus of the macaque monkey amygdala: A retrograde tracing study. J Comp Neurol 2000; 421: 52-79.

106. Guldin WO, Markowitsch HJ. Cortical and thalamic afferent connections of the insular and adjacent cortex of the cat. J Comp Neurol 1984; 229: 393–418.

107. Craig AD. Forebrain emotional asymmetry: a neuroanatomical basis? Trends Cogn Sci (Regul Ed) 2005; 9: 566-571.

108. Ochner CN, Green D, van Steenburgh JJ, Kounios J, Lowe MR. Asymmetric prefrontal cortex activation in relation to markers of overeating in obese humans. Appetite 2009; 53: 44-49.

109. Watkins KE, Paus T, Lerch JP, Zijdenbos A, Collins DL, Neelin P, et al. Structural asymmetries in the human brain: a voxel based statistical analysis of 142 MRI scans. Cereb Cortex 2001; 11: 868-877.

110. Cao Y, Whalen S, Huang J, Berger KL, DeLano MC. Asymmetry of subinsular anisotropy by in vivo diffusion tensor imaging. Hum Brain Mapp 2003; 20: 82-90.

111. Johansen-Berg H, Behrens TEJ, Sillery E, Ciccarelli O, Thompson AJ, Smith SM, et al. Functional–anatomical validation and individual variation of diffusion tractography-based segmentation of the human thalamus. Cereb Cortex 2005; 15: 31-39.

112. Croxson PL, Johansen-Berg H, Behrens TEJ, Robson MD, Pinsk MA, Gross CG, et al. Quantitative investigation of connections of the prefrontal cortex in the human and macaque using probabilistic diffusion tractography. J Neurosci 2005; 25: 8854-8866.

113. Kievit J, Kuypers H. Organization of the thalamo-cortical connexions to the frontal lobe in the rhesus monkey. Exp Brain Res 1977; 29: 299-322.

114. Barbas H, Henion THH, Dermon CR. Diverse thalamic projections to the prefrontal cortex in the rhesus monkey. J Comp Neurol 1991; 313: 65-94.

115. Giguere M, Goldman-Rakic PS. Mediodorsal nucleus: Areal, laminar, and tangential distribution of afferents and efferents in the frontal lobe of rhesus monkeys. J Comp Neurol 1988; 277: 195-213.

116. Aggleton JP, Mishkin M. Projections of the amygdala to the thalamus in the cynomolgus monkey. J Comp Neurol 1984; 222: 56-68.

117. Gower EC. Efferent projections from limbic cortex of the temporal pole to the magnocellular medial dorsal nucleus in the rhesus monkey. J Comp Neurol 1989; 280: 343-358.

118. Yeterian EH, Pandya DN. Corticothalamic connections of paralimbic regions in the rhesus monkey. J Comp Neurol 1988; 269: 130-146.

119. Markowitsch HJ, Irle E, Streicher M. The thalamic mediodorsal nucleus receives input from thalamic and cortical regions related to vision. Neurosci Lett 1982; 32: 131-136.

120. Masterman DL, Cummings JL. Frontal-subcortical circuits: the anatomic basis of executive, social and motivated behaviors. J Psychopharmacol 1997; 11: 107-114.

121. Draganski B, Kherif F, Kloppel S, Cook PA, Alexander DC, Parker GJM, et al. Evidence for segregated and integrative connectivity patterns in the human basal ganglia. J Neurosci 2008; 28: 7143-7152.

122. Metzger CD, Eckert U, Steiner J, Sartorius A, Buchmann JE, Stadler J, et al. High field fMRI reveals thalamocortical integration of segregated cognitive and emotional processing in mediodorsal and intralaminar thalamic nuclei. Front Neuroanat 2010; 4: 138.

123. Tekin S, Cummings JL. Frontal–subcortical neuronal circuits and clinical neuropsychiatry: An update. J Psychosom Res 2002; 53: 647-654.

124. Liang P, Wang Z, Yang Y, Jia X, Li K. Functional disconnection and compensation in mild cognitive impairment: evidence from DLPFC connectivity using resting-state fMRI. PLoS ONE 2011; 6: e22153.

125. Behrens TEJ, Berg HJ, Jbabdi S, Rushworth MFS, Woolrich MW. Probabilistic diffusion tractography with multiple fibre orientations: What can we gain? Neuroimage 2007; 34: 144-155.

126. Lee, Ho Yun N, Dong Gyu S, InChan L, Dong Hoon S, Hyung Suk K, et al. Diffusion-Tensor Imaging for Glioma Grading at 3-T Magnetic Resonance Imaging: Analysis of Fractional Anisotropy and Mean Diffusivity. J Comput Assist Tomogr 2008; 32: 298-303.

127. Ferda J, Kastner J, Mukenšnabl P, Choc M, Horemužová J, Ferdová E, et al. Diffusion tensor magnetic resonance imaging of glial brain tumors. Eur J Radiol 2010; 74: 428-436.

128. Arvinda H, Kesavadas C, Sarma P, Thomas B, Radhakrishnan V, Gupta A, et al. Glioma grading: sensitivity, specificity, positive and negative predictive values of diffusion and perfusion imaging. J Neurooncol 2009; 94: 87-96.

129. Galban CJ, Chenevert TL, Meyer CR, Tsien C, Lawrence TS, Hamstra DA, et al. The parametric response map is an imaging biomarker for early cancer treatment outcome. Nat Med 2009; 15: 572-576.

130. Ellingson BM, Malkin MG, Rand SD, Connelly JM, Quinsey C, LaViolette PS, et al. Validation of functional diffusion maps (fDMs) as a biomarker for human glioma cellularity. J Magn Reson Imaging 2010; 31: 538-548.

131. White ML, Zhang Y, Yu F, JaffarKazmi SA. Diffusion tensor MR imaging of cerebral gliomas: evaluating fractional anisotropy characteristics. Am J Neuroradiol 2011; 32: 374-381.

132. Li G, Yang J, Ye C, Geng D. Degree prediction of malignancy in brain glioma using support vector machines. Comput Biol Med 2006; 36: 313-325.

Author's publications used for the PhD thesis

1. Jakab A, Molnar P, Bogner P, Beres M, Berenyi E. Connectivity-based parcellation reveals interhemispheric differences in the insula. Brain Topogr 2011; *In press.* DOI: 10.1007/s10548-011-0205-y
   (IF: 3.288)

2. Jakab A, Molnar P, Emri M, Berenyi E. Glioma grade assessment by using histogram analysis of diffusion tensor imaging-derived maps. Neuroradiology 2011; 53: 483-491.
   (IF: 2.87)

Author's other publications

1. Jakab A, Blanc R, Berenyi E, Szekely G. Generation of Individualized Thalamus Target Maps by Using Statistical Shape Models and Thalamocortical Tractography. Americal Journal of Neuroradiology; *In press.* DOI: 10.3174/ajnr.A3140.
   (IF: 3.464)
2. Szakszon K, Berényi E, Jakab A, Bessenyei B, Balogh E, Köbling T, et al. Blepharophimosis mental retardation syndrome Say-Barber/Biesecker/Young-Simpson type? New findings with neuroimaging. American Journal of Medical Genetics Part A 2011; 155: 634-637.
   (IF: 2.505)

Citable conference proceedings, posters or short papers

1. Jakab A, Blanc R, Morel A, Berenyi E, Szekely G. Connectivity-augmented surgical targeting: individualization of a mean three-dimensional atlas of the human thalamus. "Proceedings of the European Society of Neuroradiology (ESNR) Congress" in Neuroradiology 2011; 53(Supplement 1): 1-2.

2. Jakab A, Béres M, Spisák T, Kis SA, Emri M, Berényi E, Handedness and interhemispheric differences in the anatomical connectivity of perisylvian language areas: a network-based approach. "Proceedings of the Annual Meeting of the European Society for Magnetic Resonance in Medicine and Biology" in Mag. Res. Mat. Phys 2011; 24 (S1): 276.

3. Jakab A, Blanc R, Werner B, Martin E, Morel A, Székely G. Connectivity mapping of the thalamus: implementation for targeting in transcranial high-intensity focused ultrasound surgery. “Proceedings of the 13rd World Congress of Ultrasound in Medicine and Biology” in Ultrasound in Medicine & Biology 2011; 37(Supplement). doi:10.1016/S0301-5629(11)01229-4

4. Jakab A, Berenyi E, Molnar PP. Imaging and morphology: current options in seizure diagnostics. “Proceedings of the 111th Meeting of the British Neuropathological Society” in Neuropathology and Applied Neurobiology 2010; 36(Suppl. 1).

5. Jakab A, Berenyi E, Molnar PP. Preoperative diffusion imaging-derived data in prediction of glioma grades. “Abstracts of the XVIIth International Congress of Neuropathology (ICN 2010)” in Brain Pathology 2010; 20: 1-107.

6. Berenyi E, Jakab A, Emri M, Molnar PP. Comparative analysis of water diffusion imaging and histopathological features of gliomas: is noninvasive grading feasible? “Proceedings of the 111th Meeting of the British Neuropathological Society” in Neuropathology and Applied Neurobiology 2010; 36(Suppl. 1).

7. Spisák T, Koselák M, Opposits G, Kis SA, Trón L, Jakab A, Berényi E, Emri M, Region management toolkit for atlas-space image processing. “Proceedings of the Annual Meeting of the European Society for Magnetic Resonance in Medicine and Biology” in Mag. Res. Mat. Phys 2011; 24 (S1): 543.

8. Spisák T, Koselak M, Opposits G, Kis S, Tron L, Jakab A, Berenyi E, Emri M. Digital brain atlas assisted localization software for individual and population analysis of SPECT and PET data. European Journal of Nuclear Medicine &Moleular Imaging 2011; 38(S2): 258.

9. Opposits G, Spisak T, Lajtos I, Pohubi L, Galuska L, Jakab A, Berenyi E, Emri M. Automated region analysis of brain PET examinations. European Journal of Nuclear Medicine &Moleular Imaging 2011; 38(S2): 333.

Register Number: DEENKÉTK /99/2012.
Item Number:
Subject: Ph.D. List of Publications

Candidate: András Jakab

Neptun ID: CH3MWN

Doctoral School: Doctoral School of Neurosciences

List of publications related to the dissertation

1. **Jakab, A.**, Molnár, P., Emri, M., Berényi, E.: Glioma grade assessment by using histogram analysis of diffusion tensor imaging-derived maps.
Neuroradiology. 53 (7), 483-491, 2011.
DOI: http://dx.doi.org/10.1007/s00234-010-0769-3
IF:2.87 (2010)

2. **Jakab, A.**, Molnár, P.P., Bogner, P., Béres, M., Berényi, E.: Connectivity-based parcellation reveals interhemispheric differences in the insula.
Brain Topogr. Epub ahead of print (2011)
DOI: http://dx.doi.org/10.1007/s10548-011-0205-y
IF:3.288 (2010)

List of other publications

3. **Jakab, A.**, Béres, M., Spisák, T., Kis, S.A., Emri, M., Berényi, E.: Handedness and interhemispheric differences in the anatomical connectivity of perisylvian language areas: A network-based approach.
Magn. Reson. Mater. Phy. 24 (Suppl. 1), 276. p., 2011.

4. Opposits, G., Spisák, T., Lajtos, I., Pohubi, L.Z., Galuska, L., **Jakab, A.**, Berényi, E., Emri, M.: Automated region analysis of brain PET examinations.
Eur. J. Nucl. Med. Mol. Imaging. 38 (Suppl. 2), S333. p., 2011.
DOI: http://dx.doi.org/10.1007/s00259-011-1911-0

5. Spisák, T., Koselák, M., Opposits, G., Kis, S.A., Trón, L.K., **Jakab, A.**, Berényi, E., Emri, M.: Region management toolkit for atlas-space image processing.
Magn. Reson. Mater. Phy. 24 (Suppl. 1), 543-543, 2011.

6. Spisák, T., Koselák, M., Opposits, G., Kis, S.A., Trón, L.K., **Jakab, A.**, Berényi, E., Emri, M.: Digital brain atlas assisted localization software for individual and population analysis of SPECT and PET data.
Eur. J. Nucl. Med. Mol. Imaging. 38 (Suppl. 2), S258. p., 2011.
DOI: http://dx.doi.org/10.1007/s00259-011-1910-1

7. Spisák, T., Opposits, G., **Jakab, A.**, Koselák, M., Kis, S.A., Trón, L., Berényi, E., Emri, M.: Anatomical localization software for individual and population analysis of PET data.
Nucl. Med. Rev. Cent. East. Eur. 14 (Suppl. A.), A15. p., 2011.

8. Szakszon, K., Berényi, E., **Jakab, A.**, Bessenyei, B., Balogh, E., Köbling, T., Szilvássy, J., Knegt, A.C., Oláh, É.: Blepharophimosis mental retardation syndrome Say-Barber/Biesecker/Young-Simpson type - New findings with neuroimaging.
Am. J. Med. Genet. A. 155 (3), 634-637, 2011.
DOI: http://dx.doi.org/10.1002/ajmg.a.33837
IF:2.505 (2010)

Total IF: 8.663

Total IF (publications related to the dissertation): 6.158

The Candidate's publication data submitted to the Publication Database of the University of Debrecen have been validated by Kenezy Life Sciences Library on the basis of Web of Science, Scopus and Journal Citation Report (Impact Factor) databases.

26 March, 2012

Keywords

Magnetic resonance imaging; diffusion weighted imaging; diffusion tensor imaging; biomedical image processing; neuroanatomy; insula; thalamus; glioma; tumor histopathology

Tárgyszavak

Mágneses rezonanciás képalkotás; diffúzió súlyozott képalkotás; diffúziós tenzor képalkotás; orvosi képfeldolgozás; neuroanatómia; insula; thalamus; glioma; tumor hisztopatológia

Acknowledgements

I am grateful first of all to my supervisor, Dr. Ervin Berényi who has been the leader of my research studies for the majority of my studentship. My first scientific explorations were possible primarily due to his ability to motivate and that his breadth of view exceeds far beyond the everyday routine of radiological clinical practice. He started a laboratory for biomedical imaging and image processing at the University of Debrecen, Medical and Health Sciences Center in which I could pursue research without major boundaries. Herein I acknowledge the fruitful collaboration with Prof. Dr. Péter Molnár who not only shared his powerful know-how on brain glioma pathology but sharpened my sense of critical reading and scientific writing of high standards.

I also thank the former colleagues and my supervisor Prof. Dr. Gábor Székely from the Swiss Federal Institution of Technology, Computer Vision Laboratory for hosting me and working with me for a very productive period. I acknowledge the help of Dr. Anne Morel on the exploration of the classical neuroanatomy of the insula and thalamus and also her valuable comments on my journal publications on such topics. I thank for Prof. Ernst Martin and Beat Werner for hosting me at the Focused Ultrasound Laboratory, University Children's Hospital of Zürich where I could apply my theoretical knowledge of biomedical image processing to the benefit of patients undergoing image guided thalamotomies.

I am grateful to my parents and my girlfriend for supporting and helping me not only during this exciting period but all through my life.

Appendix